Summer 8-1-2023

# A Comparison of Fixed Versus Moving Eulerian Meshes for 1-D Radiative Shock Problems

Dylan Weatherred

**Dylan Weatherred**

*Candidate*

**Nuclear Engineering**

*Department*

This thesis is approved, and it is acceptable in quality and form for publication:

*Approved by the Thesis Committee:*

Cassiano Endres De Oliveira

Eric Lang

HyeongKae Park

# A Comparison of Fixed Versus Moving Eulerian Meshes for 1-D Radiative Shock Problems

**BY**

**Dylan Weatherred**
B.S., Nuclear Engineering, University of New Mexico, 2021

THESIS

Submitted in Partial Fulfillment
of the Requirements for the Degree of
**Master of Science**

**Nuclear Engineering**
The University of New Mexico
Albuquerque, New Mexico

**August, 2023**

## DEDICATION

I would first like to thank my parents for their constant support. It is their love and support that kept me motivated. Thank you for always believing in me. I would also like to thank my partner Alexandria. Thank you for always pushing me to be the best that I can be. I can't wait to see what the future holds for us.

## ACKNOWLEDGMENTS

I would like to thank my mentor Dr. HyeongKae Park. Through all of my questions and times where I was stuck you were always able to answer or point me in the right direction. I appreciate your guidance and patients. I would also like to thank my research advisor Professor Cassiano Endres De Oliveira. Thank you for always answering my questions, providing direction when I was confused, and all of the books and resources you provided. Your support was instrumental in my success.

# A Comparison of Fixed Versus Moving Eulerian Meshes for 1-D Radiative Shock Problems

**by**

**Dylan Weatherred**

**B.S., Nuclear Engineering, University of New Mexico, 2021**

**M.S., Nuclear Engineering, University of New Mexico, 2023**

## Abstract

Testing codes used to solve the radiation-hydrodynamics equations requires the use of radiative shock problems. These problems contain stiff shocks and test the coupling of the material motion and the energy exchange between the radiation and material. However, these problems are difficult to solve due to large differences in time scale between radiation and material equations, resolving shocks, and modeling radiation and material interactions. This thesis will look to solve radiative shock problems in 1-D using the Eulerian formulation on fixed and moving meshes. The moving mesh method proposed takes advantage of the more simple Eulerian formulation of the radiation hydrodynamics equations and the ability to handle large deformations, while also benefiting from the Lagrangian frame regarding shock resolution and material interfaces. The methods are compared using a Sod shock tube problem to test the hydrodynamics, Marshak wave to test the radiative solver, and 3 radiative shock problems. The radiative shock problems will be two stationary shocks with Mach numbers of 1.2 and 3.0, and one moving shock with a Mach number of 1.2.

## TABLE OF CONTENTS

# 1 Introduction

## 1.1 High Energy Density Physics

High-energy-density physics is a branch of physics that studies how matter behaves under extreme temperatures and pressures. These pressures range from 1 Mbar to 1000 Gbar and temperatures in excess of 100 eV. Experimentally, scientists use high-power lasers, particle accelerators, and other advanced experimental tools to create extremely high temperatures and pressures. By understanding the behavior of materials and matter under these conditions, scientists are able to gain insights into the fundamental physics of the universe. Applications of high-energy-density physics are wide-ranging and include nuclear fusion, astrophysics, plasma physics, and materials science. High-energy-density physics is a rapidly evolving field that has the potential to transform the understanding of the universe and the ability to develop new technologies.

## 1.2 Inertial Confinement Fusion

For energy production, fusion is usually achieved by utilizing either magnetic or inertial confinement. Magnetic confinement relies on magnets to control the shape of the plasma in which fusion takes place. In inertial confinement, the plasma is controlled by the inertial force of the collapsing fuel. The focus of this work will primarily be related to inertial confinement fusion. Inertial confinement fusion uses lasers to deposit energy into the fuel targets in order of fusion to occur. This is done by two main methods which are referred to as direct or indirect drive. In direct drive ICF, the laser is set directly incident on the fuel target. However, with this method, uniform heating of the fuel target is difficult which constrains the beam energy and fuel capsule size. For example, if a beam energy of 1 mJ is being used, the fuel capsule is limited to just 2mm in diameter to ensure uniform heating. When using indirect drive, the fuel target is placed inside a container called a hohlraum. The hohlraum lined with a heavy metal

such as gold and the laser are then set incident on the lined wall of the hohlraum heating the heavy metals. Once heated, the heavy metals will emit x-rays which, in turn, begin to heat the fuel capsule. However, this method is not without its disadvantages. To heat the hohlraum to a high enough temperature to produce x-rays requires a significant amount of energy. If the system is trying to be used for energy production, a higher amount of input energy will make it harder to get to full break even and energy production. Figure 1 shows a comparison of the indirect and direct drive methods.

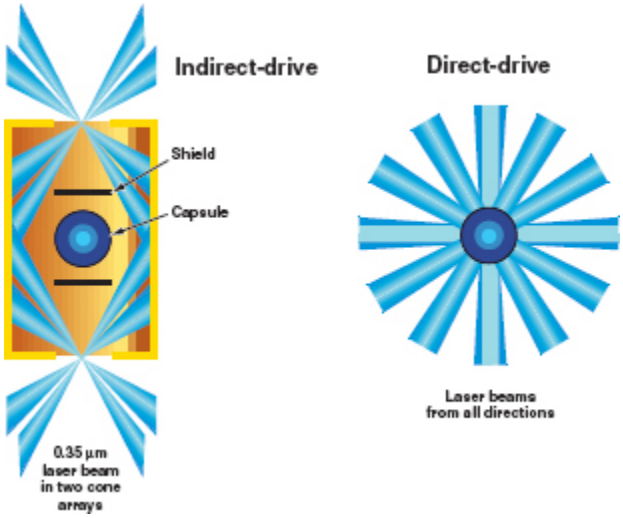


Figure 1: Direct vs Indirect ICF target examples [1].

While the energy transfer mechanism differ between the two methods, the actual fusion process is the same. Once enough energy has been deposited into the outer layer of the fuel capsule it will explode. As a result of this explosion, shock waves will transfer throughout the fuel compressing it. There needs to be enough compression such that the electrostatic force, which keeps the atoms separated, can be overcome by the nuclear force. The energy required for fusion is known as the Coulomb Fusion Barrier. It is directly related to the electrical charge of the nuclei being used. Due to its low electrical charge, hydrogen is the easiest to fuse, so the fuel targets generally contain deuterium ($H^2$) and tritium ($H^3$) which fuse at a distance of just 1 Femtometer [2]. This compression of the fuel from the resulting shock means it is critical to ensure that the

capsule is being heated evenly from all sides. Any asymmetrical heating of the capsule can lead to instabilities in the plasma such as the Rayleigh–Taylor instability [10]. Lawrence Livermore National Laboratory (LLNL) started some of the early research into ICF in the late 1950's. Starting with computer simulations, by the early 1960's, they were able to perform a full simulation using 1 mg of D-T fuel inside of a dense shell [16]. However, this was before the invention of the laser so other driving mechanism had to be researched. These methods include pulsed power machines, charged particle accelerators, plasma guns, and hypervelocity pellet guns. After the invention of the laser, there was a significant growth in research surrounding ICF. Following its invention, one of the earliest, large-scale ICF attempts was done at LLNL with the Shiva laser. This was a 20-beam neodymium doped glass laser that started operation in 1978. It was designed as a proof of concept to demonstrate compression of fusion capsules to densities much greater than that of the liquid density of Hydrogen. While fusion yields were low, Shiva was able to reach 100x the liquid density of Hydrogen [9]. As technology advances so does the research surrounding ICF. The National Ignition Facility (NIF) at LLNL, with its 192 beam design, was able to achieve break-even ignition on December 5, 2022 [5].

### 1.3 Hydrodynamics

Hydrodynamics is one of the many subdisciplines which is specifically interested in studying fluid in motion. The founding principles of hydrodynamics are the conservation equations, specifically, conservation of mass, conservation of linear momentum, and conservation of energy. The conservation of mass states that the mass rate of change inside a control volume $V$, must be equal to the net rate of fluid flow into that control volume [3]. Simply put, this means that mass cannot be created or destroyed within the control volume. This can be shown with the integral form of the continuity equa-

tion as shown by equation 1.3.1

$$\frac{\partial}{\partial t}\iiint_V \rho dV = -\oiint_S \rho u \cdot dS \tag{1.3.1}$$

where $S$ denotes the surface of control volume $V$, the fluid density is denoted by $\rho$, the fluid velocity vector is $u$, and $t$ represents time.

The conservation of momentum states that any net rate of change in the momentum of the fluid is due to the net flow of momentum into the volume and external forces acting on the fluid within the volume. As was done with the conservation of mass, the conservation of momentum will be expressed using the integral form of the continuity equation.

$$\frac{\partial}{\partial t}\iiint_V \rho u dV = -\oiint_S (\rho u \cdot dS)u - \oiint_S P dS + \iiint_V \rho f_{body} dV + F_{surf} \tag{1.3.2}$$

The first term on the right-hand side of equation 1.3.2 represents the net rate of momentum convected into the volume, the second term force due to pressure of the surface of the volume where $P$ is the material pressure, the third term is the net acceleration of the mass due to any body forces which is denoted by $f_{body}$, and the fourth term accounts for any surface forces such as viscous forces which is denoted by $F_{surf}$.

Lastly, the conservation of energy states that while energy can be converted within the control volume, the total energy must remain the same. One example of this is viscous dissipation in which the mechanical energy of the fluid is converted to heat. The integral form of the conservation of total energy can be seen in equation 1.3.3

$$\iiint_V \frac{\partial E}{\partial t} dV = -\oiint_S E u \cdot dS + \oiint_S P u \cdot dS - \oiint_S q \cdot dS \tag{1.3.3}$$

where $E$ is the total energy and $q$ is the rate at which some external source of energy is added to the system, generally through heating the surface $S$.

One way to numerically model hydrodynamics through the use of the Eulerian form of the conservation equations also known as the conservation form. These equations, named after Leonhard Euler, are a set of quasilinear partial differential equations which govern adiabatic and inviscid flow. They are related to the Navier-Stokes equations with zero viscosity and thermal conductivity. Historically, the conservation of mass and momentum equations were derived by Euler, but the full set of balance equations, including conservation of energy, are often credited to Euler in literature. In conservation form, the Euler equations can be expressed as follows

$$\frac{\partial U}{\partial t} + \nabla \cdot F = 0 \tag{1.3.4}$$

where

$$U = \begin{pmatrix} \rho \\ \rho u \\ \rho E \end{pmatrix} \quad \& \quad F = \begin{pmatrix} \rho u \\ \rho u u + P \\ \rho E u + P u \end{pmatrix} \tag{1.3.5}$$

### 1.4 Radiative Transport

Radiative transport is the study of the energy transfer of electromagnetic radiation as it propagates through a medium. As radiation propagates through a material, absorption, scattering, and emission processes will affect the radiation flux, its energy, and its direction of travel. This is expressed mathematically using the radiative transfer equation, which shows as a beam of radiation travels, it looses energy due to absorption, gains energy from emission, and redistributes energy via scattering [6]. From the radiative transport equation, there are a number of methods that can be used to numerically solve the equation. The fundamental quantity of radiative transport is the specific intensity which is denoted as $I_\nu$. The specific intensity is a function of position $r$, time $t$, direction $\Omega$, and frequency $\nu$ and can be expressed as $I_\nu(r, t, \Omega, \nu)$. The amount of energy which is transported across a surface element $dS$, by radiation with frequencies

$(\nu \rightarrow \nu')$, where $\nu' = \nu + d\nu$ is given by equation 1.4.1.

$$dE_\nu = I_\nu(r, \Omega, t)\, cos\theta\, dS\, d\Omega\, \Delta\nu\, \Delta t \tag{1.4.1}$$

where $\theta$ is the angle between the the direction of travel $\Omega$ and the normal to the surface of $dS$. The intensity uses power units, which is energy per unit time, but also takes into account changes per solid angle and frequency bandwidth. In centimeter, gram, and second (cgs) units, this is expressed as $erg\, cm^{-2}\, s^{-1}\, Hz^{-1}\, sr^{-1}$.
To derive the transport equation, it can be useful to start by looking at a bundle of radiation. If the radiation does not interact with the matter it passes through, the bundle of radiation with total energy $I_\nu\, cos\theta\, dS\, d\Omega\, \Delta\nu\, \Delta t$ will have the same total energy at time $t + \Delta t$, occupy the same frequency bandwidth $\Delta\nu$, and the same solid angle $d\Omega$ while being in a different position r. Since photons move at the speed of light, it can shown that the intensity at time $t + \Delta t$ equals the initial intensity of radiation packet.

$$I_\nu(r + \Omega c\Delta t, \Omega, t + \Delta t) = I_\nu(r, \Omega, t) \tag{1.4.2}$$

It is then possible to perform a Taylor expansion of the left hand side of the equation about the point $r$ and time $t$. After performing the expansion, any terms which are on the order of $\Delta t^2$ or higher can be canceled out, the $I_\nu(r, n, t)$ term can be subtracted out, and then divide by $c\Delta t$. This gives the radiation transport equation, without any sources or sinks, as shown in equation 1.4.3.

$$\frac{1}{c}\frac{\partial I_\nu}{\partial t} + \Omega \cdot \nabla I_\nu = 0 \tag{1.4.3}$$

Now that the most simple form of the radiative transport equation has been defined, it is now important to discuss the scattering, absorption, and emission processes which affect the radiation as it moves through the material. It is often easiest to start by con-

sidering the absorption term and then the emission term. To understand the absorption term, it can be useful to think of a beam of radiation which is set incident on a slab with a thickness of $L$. As the radiation passes through the slab, some of the radiation is attenuated. Figure 2 below roughly shows this by showing a decrease in the intensity of the radiation after it has passed through the slab.

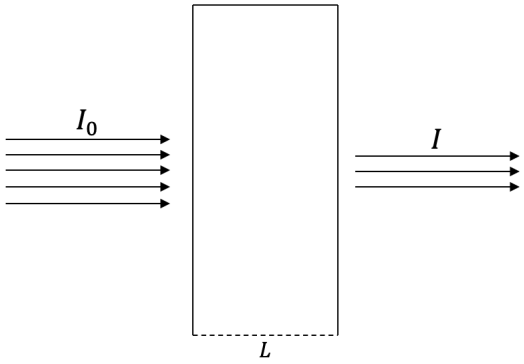


Figure 2: Example of radiation attenuation through a slab.

If none of the absorbed energy is replaced, the change in the radiation intensity can be calculated using equation 1.4.4.

$$\Delta I_\nu = -\sigma_{a,\nu} c \Delta t I_\nu \tag{1.4.4}$$

In this equation, $\sigma_{a,\nu}$ is the absorption coefficient for photons with a frequency of $\nu$, and has units of inverse length. If this is applied to a thick slab $L >> c\,\Delta t$ the radiation intensity is calculated by equation 1.4.5.

$$I_\nu = I_\nu^0 exp(-\sigma_{a,\nu} L) \tag{1.4.5}$$

For slabs that are thin ($L \leq c\,\Delta t$), there is a $\sigma_{a,\nu} c \Delta t$ probability of interaction, and a $1 - \sigma_{a,\nu} c \Delta t$ probability of no interaction with the slab. In this case, the change in intensity is $\sigma_{a,\nu} c \Delta t I_\nu$ as defined above.

The emissivity of the radiation determines how much energy is deposited into the slab

as the radiation passes through it. It is a function of the slab thickness $L$, but does not depend on the beam intensity similar to absorption. The change in the radiation intensity due to emission using equation is given 1.4.6.

$$\Delta I_\nu = j_\nu c \Delta t \tag{1.4.6}$$

The emissivity or emission coefficient is represented using $j_\nu$. However, unlike the absorption coefficient which has units of inverse length, the emission coefficient has units of $I_\nu$ per unit length which becomes energy per unit volume, per unit frequency bandwidth, per solid angle, per time. If the absorption and emission terms are included in equation 1.4.2, the Taylor expansion can be done again, canceling out terms with $\Delta t^2$ or higher, and divide out $c\Delta t$ to get the next form of the radiative transport equation.

$$\frac{1}{c}\frac{\partial I_\nu}{\partial t} + \Omega \cdot \nabla I_\nu = j_\nu - \sigma_{a,\nu} I_\nu \tag{1.4.7}$$

Now that the effects of absorption and emission on the transport equation have been accounted for, the effect of scattering can now be included. For simplicity, it is assumed isotropic and coherent scattering and resulting equation is:

$$\frac{1}{c}\frac{\partial I_\nu}{\partial t} + \Omega \cdot \nabla I_\nu = j_\nu + \frac{\sigma_{s,\nu}}{4\pi}\int I_\nu d\Omega' - (\sigma_{a,\nu} + \sigma_{s,\nu}) I_\nu \tag{1.4.8}$$

## 1.5 Radiation Hydrodynamics

To couple the hydrodynamics and radiative transport physics described above requires the equations of radiation hydrodynamics. These equations describe the propagation of thermal-radiation through the fluid, the hydrodynamics which describe the fluid motion, the effect of the radiation on the hydrodynamics, and the momentum of the fluid on the radiation. This work is specifically interested in thermal-radiation as this is electromagnetic radiation of atomic origin rather than nuclear. The importance of

the thermal radiation on the problem is directly proportional to increasing temperature. This is due to the Planck distribution of the radiation energy density varying as the temperature to the fourth power. For example, at room temperature, radiation effect can be ignored. However, at temperatures around a million degrees, the radiation field can become comparable to or dominate the fluid energy and momentum densities [17]. There are situations in which the radiation can be ignored even if the temperature suggests strong radiation effects should be present. One example is deep within stars or other celestial bodies. In these regions, the mean free path of the photon is negligible when compared with the size of the system. This is due to the distance the fluid must travel in order for any change to occur being much larger than the distance the radiation travels [6].

When proper coupling is required, solving the radiation hydrodynamics equations is challenging for a number of reasons. The timescales required to solve the radiation and hydrodynamics equations are separated by many orders of magnitude. This can lead to instability when solving the radiation equations and often requires the radiation terms to be implicitly solved for. Another challenge when solving the radiation hydrodynamics equations is properly resolving shocks. This often requires high order schemes which have been extensively explored for the Euler equations and radiative transport/diffusion equations. However, coupling these schemes together presents its own challenges. Lastly, handling material interfaces for multi-material problems is very important due to the interaction of the radiation with the material.

### 1.6 Fixed Versus Moving Eulerian Meshes

When formulating the equations for radiation hydrodynamics there are two traditional reference frames which are used: the Eulerian frame and the Lagrangian frame. In the Eulerian frame, a static mesh is placed over the problem domain. The time derivative is then taken in a fixed point in inertial space. The formulation in the Eulerian frame

is somewhat more simple; however, it does require a flux term for the conserved values across the fixed cell boundaries. One of the benefits to the Eulerian frame is its ability to handle large deformations without the risk of mesh tangling. However, it can struggle to resolve shocks, especially when using first order methods. In the Lagrangian frame, rather than placing a fixed mesh over the problem domain, the mesh moves and deforms with the fluid. This allows for better shock resolution and the ability to adequately handle material interfaces. However, the formulation requires slightly more effort and large deformations or complex fluid flow can cause mesh tangling [6].

This work proposes a different frame to the Eulerian and Lagrangian frames which will be referred to as moving mesh Eulerian. The moving mesh Eulerian frame utilizes the more simple Eulerian formulation of the radiation hydrodynamics equations, while utilizing the moving mesh from the Lagrangian frame. However, unlike the Lagrangian frame where the mesh moves at the same velocity of the fluid, the mesh velocity is arbitrary in the moving mesh Eulerian frame. The arbitrary mesh speed can allow better shock resolution, prevent mesh tangling, and handle large deformations in the material. A simple example of how the fixed and moving meshes work can be seen in Figure 3 below. This figure shows a block of fluid which is initially stationary in the grid. Some arbitrary fluid flow is applied moving from the left to the right. In the fixed mesh case, it is shown that the flow causes the fluid to move within the grid but the grid itself does not change. However, in the moving mesh case, as the fluid moves within the mesh, the mesh moves as well as some function of the fluid velocity.

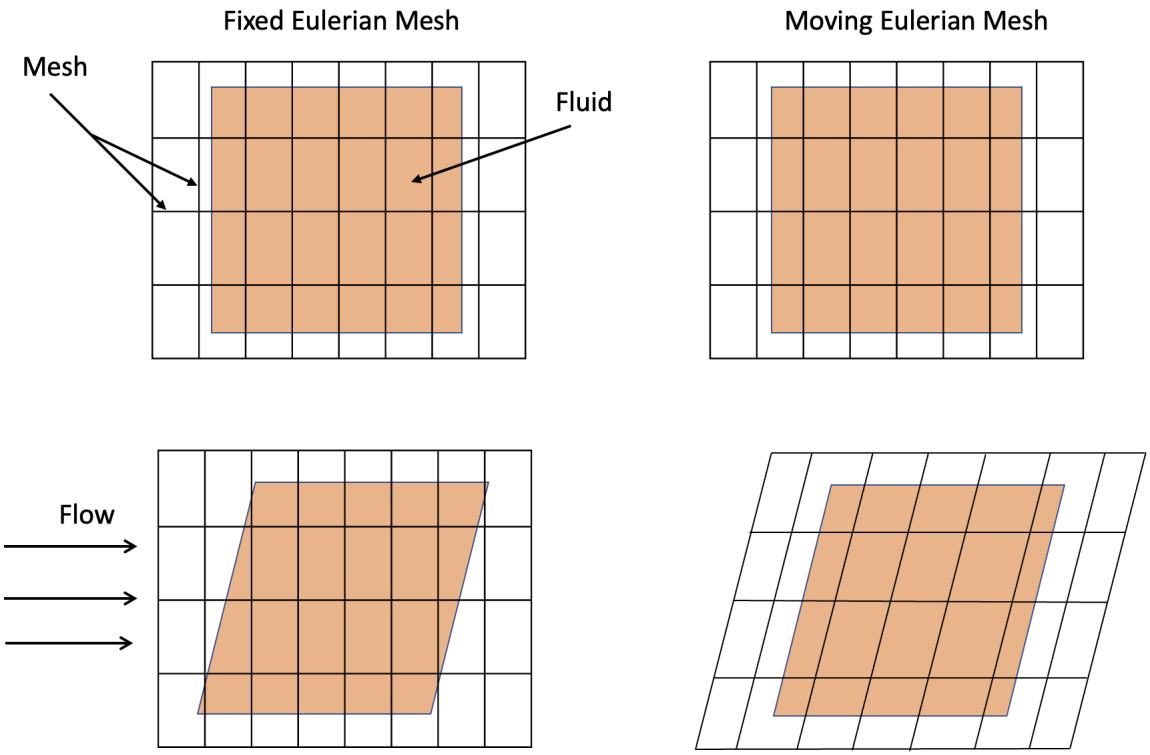


Figure 3: Example of fixed versus moving Eulerian meshes. The top shows the fluid and mesh at $t = 0$, and the bottom shows the fluid and mesh at some final time $t = t_f$.

Some work has been done with radiation hydrodynamics on moving meshes by Kannan et al. [12], Springel [20], and Chang et al. [7]. However, these works are primarily focused on astrophysics rather than inertial confinement fusion. In astrophysics, the size and timescale of the problems are significantly larger. This can reduce some of the difficulty and computational cost of modeling the radiative transport as it can allow for larger time steps and for the use of explicit methods. These works also use a Voronoi tessellation to define their meshes. While this allows them to deal with mesh tangling, the setup cost compared to an Eulerian mesh is large. There are also complex physics that occur in astrophysics that do not need to account for in ICF. Some examples of these include infrared dust–gas coupling, self-gravity and, in some cases, the use of magnetohydrodynamics equations.

# 2 Methodology

## 2.1 Fixed Mesh Eulerian

In the Eulerian frame on a fixed mesh, the following four equations are what need to be solved.

$$\frac{\partial \rho}{\partial t} = -\nabla \cdot (\rho u) \tag{2.1.1}$$

$$\frac{\partial u\rho}{\partial t} = -\nabla \cdot (\rho u^2 + P) \tag{2.1.2}$$

$$\frac{\partial E}{\partial t} = \nabla \cdot D\nabla E_r - \nabla \cdot [(E + P)u] \tag{2.1.3}$$

$$\frac{\partial E_r}{\partial t} = \nabla \cdot D\nabla \cdot E_r + \sigma acT^4 - \sigma cE_r - \nabla(E_r u) - p_r \nabla \cdot u \tag{2.1.4}$$

In these equations, $\rho, u, E$, and $P$ are the density, velocity, total energy, and total pressure. The total energy can be found by $E = \rho(e_i + u^2/2) + E_r$ where $e_i$ denotes the specific internal energy and the total pressure can be found by $P = p_h + p_r$. Hydrodynamics properties are denotes with the subscript $h$ and radiation properties with subscript $r$. The hydro specific total energy is found by $E_h = e_i + u^2/2$. This allows the total energy to be expressed as $E = \rho E_h + E_r$. Substituting this expression into equation 2.1.3 and subtracting equation 2.1.4 yields the following total hydro energy equation.

$$\frac{\partial \rho E_h}{\partial t} = \sigma cE_r - \sigma acT^4 - \nabla \cdot [(\rho E_h + P)u] + p_r \nabla \cdot u \tag{2.1.5}$$

## 2.2 Moving Mesh Eulerian

Although the moving mesh method utilizes the Eulerian form of the radiation-hydrodynamics equations, the equations need to be transformed to account for a non-uniform mesh. To do this, the rate of change integrals of a function over a moving volume that is occupied by a fluid must be considered. First, consider a "material volume" that perma-

nently contains the same particles $V_t$, that is bound by a smooth surface $S_t$, and moves with a velocity of $u(r,t)$. The material time derivative of the integral of a scalar function $f(r,t)$, over the time-varying material volume $V_t$, is expressed by Reynolds transport theorem.

$$\frac{d}{dt}\int_{V_t} f(r,t)dV = \int_{V_c \equiv V_t} \frac{\partial f(r,t)}{\partial t} dV + \int_{S_c \equiv S_t} f(r,t)u \cdot ndS \tag{2.2.1}$$

This theorem states that the total rate of change in a function $f$, is due to the local rate of change in the control volume $V_c$, and the flux in/out of the surface $S_c$. For example, the conservation of mass which states that the total rate of change is equal to zero. e.g.,

$$\frac{d}{dt}\int_{V_t} \rho(r,t)dV = 0 \tag{2.2.2}$$

which leads to the Eulerian description:

$$\int_{V_c \equiv V_t} \frac{\partial \rho(r,t)}{\partial t} dV + \int_{S_c \equiv S_t} \rho(r,t)u \cdot ndS = 0 \tag{2.2.3}$$

$$\int_{V_c \equiv V_t} \left( \frac{\partial \rho(r,t)}{\partial t} + \nabla \cdot \rho(r,t)u \right) dV = 0 \tag{2.2.4}$$

To do this for an Arbitrary Lagrangian-Eulerian (ALE) reference frame (e.g. moving mesh Eulerian), a new volume is considered which has an arbitrary volume $V_a$, moves with velocity $w(r,t)$, and is bound by the surface $S_a$. It is important to note that the mesh speed $w(r,t)$ is measured with respect to the fixed Eulerian reference frame. The Reynolds transport theorem for this new volume now states:

$$\frac{\partial}{\partial t}\int_{V_a} f(r,t)dV = \int_{V_c \equiv V_a} \frac{\partial f(r,t)}{\partial t} dV + \int_{S_c \equiv S_a} f(r,t)w \cdot ndS \tag{2.2.5}$$

The equation above states that at some time $t$, the arbitrary volume $V_a$ coincides with the control volume $V_c$. The rate of change of $f$ in the arbitrary volume is the same as

the rate of change in the Eulerian frame, and due to the flux in/out of $f$ due to the mesh velocity $w$. Substituting $\rho$ for $f$ in equation 2.2.5, and using equation 2.2.3, gives the integral equation for conservation of mass on a moving mesh.

$$\frac{\partial}{\partial t}\int_{V_a}\rho(r,t)dV = -\int_{S_a}\rho(r,t)u\cdot ndS + \int_{S_a}\rho(r,t)w\cdot ndS \tag{2.2.6}$$

$$\frac{\partial}{\partial t}\int_{V_a}\rho(r,t)dV + \int_{S_a}\rho(r,t)(u-w)\cdot ndS = 0 \tag{2.2.7}$$

Similarly, this process can be used to find the conservation of momentum and energy equation on a moving mesh. In the Eulerian frame, the conservation of momentum is written as

$$\int_{V_c}\frac{\partial \rho u}{\partial t} + \int_{S_c}\rho u\otimes u\cdot ndS + \int_{S_c}P\ ndS = 0 \tag{2.2.8}$$

Applying Reynolds transport theorem where $f = \rho u$:

$$\frac{\partial}{\partial t}\int_{V_a}\rho u dV = \int_{V_c\equiv V_a}\frac{\partial \rho u}{\partial t}dV + \int_{S_c\equiv S_a}\rho u\otimes w\cdot ndS \tag{2.2.9}$$

Lastly, substituting 2.2.9 into 2.2.8 gives:

$$\frac{\partial}{\partial t}\int_{V_a}\rho u dV = -\int_{S_a}\rho u\otimes u\cdot ndS - \int_{S_a}P\ ndS + \int_{S_a}\rho u\otimes w\cdot ndS \tag{2.2.10}$$

$$\frac{\partial}{\partial t}\int_{V_a}\rho u dV + \int_{S_a}\rho u\otimes (u-w)\cdot ndS + \int_{S_a}P\ ndS = 0 \tag{2.2.11}$$

The conservation of energy in the Eulerian frame can be expressed as:

$$\int_{V_c}\frac{\partial \rho E}{\partial t}dV + \int_{S_c}(\rho E + p)u\cdot ndS = 0 \tag{2.2.12}$$

Applying the Reynolds transport theorem

$$\frac{\partial}{\partial t}\int_{V_a}\rho E dV = \int_{V_c\equiv V_a}\frac{\partial \rho E}{\partial t}dV + \int_{s_c\equiv S_a}\rho E w\cdot ndS \tag{2.2.13}$$

Substituting the Eulerian conservation law into the Reynolds transport theorem for the conservation of Energy gives:

$$\frac{\partial}{\partial t}\int_{V_a}\rho E dV = -\int_{S_a}(\rho E + P)u\cdot n dS + \int_{S_a}\rho E w\cdot n dS \tag{2.2.14}$$

$$\frac{\partial}{\partial t}\int_{V_a}\rho E dV + \int_{S_a}[\rho E(u-w)+Pu]\cdot n dS = 0 \tag{2.2.15}$$

After applying divergence theorem to the surface integrals and performing the integration, the general form of the conservation equation on a moving mesh can be expressed in the following form.

$$\frac{1}{V}\frac{\partial VU}{\partial t} = -\frac{\partial F}{\partial x} \tag{2.2.16}$$

where

$$U = \begin{pmatrix} \rho \\ \rho u \\ \rho E \end{pmatrix} \quad \& \quad F = \begin{pmatrix} \rho(u-w) \\ \rho u(u-w)+P \\ \rho E(u-w)+Pu \end{pmatrix} \tag{2.2.17}$$

After performing the operator splitting procedure that will be explained later, this form can be applied to the hydrodynamics equations to solve for the conserved values on a moving mesh. The non-uniformity of the mesh for the radiative transport is accounted for in the calculation of the radiative flux. A description of this can be found in appendix A.

## 2.3 The Diffusion Approximation

In section 1.4 the radiative transfer equations in differential form was shown to be:

$$\frac{1}{c}\frac{\partial I_\nu}{\partial t} + \Omega\cdot\nabla I_\nu = j_\nu + \frac{\sigma_{s,\nu}}{4\pi}\int I_\nu d\Omega' - (\sigma_{a,\nu}+\sigma_{s,\nu})I_\nu \tag{2.3.1}$$

Methods of solving the radiative transfer equations are covered extensively in literature. Castor [6] covers many methods in a way that is easily understood, and Mihalas

& Mihalas [15] provide detailed descriptions of these methods as well. There are two general approaches to numerically solving these equations: probabilistic methods and deterministic methods. Probabilistic methods, also known as Monte Carlo methods, use random sampling to determine the values of intensity, temperature, etc at some time $t$. To do this, each photon is "walked" through the problem using random numbers at each step to determine events take place. At $t = 0$ particles are "born" at a random position and given a random direction of travel. Given the particles position and direction of travel, it is then determined if the particles' first interaction will be a collision with another particle, the particle will cross the boundary of its region in space, or if it will loose all of its energy along its direction of travel within the time step $\Delta t$. If the particle will collide, it is then determined if the particle is absorbed, depositing its energy into the material, or scattered traveling in a different direction determined by a random number. At the end of the time step, the results are tallied and the intensity, temperature, radiation energy density, etc. are determined. Monte Carlo solutions have the ability to generate accurate results; however, this ability is dependent on the number of particles $N$ that are used. As the number of particles increases, the error in the solution decreases by a factor of $1/\sqrt{N}$, but the computational expense increases [6].

Deterministic methods directly solve the equations given a set of parameters and initial values for the problem. A few of the most common methods include the discrete ordinates method also known as SN methods, the method of characteristics, and the finite element method. The discrete ordinates method is among the most widely used methods for solving the radiative transport equation. It start by discretizing the radiative transport equation in both space and direction by approximating the intensity of the radiation at discrete points and directions in space and angle. For each angle, the RTE is solved separately. This method is highly accurate, especially when used for problems that are highly anisotropic. However, the computational cost can become

high in problems that are 3 dimensional or have many discrete directions. Like the discrete ordinates method, the method of characteristics follows the path of individual packets of radiation or rays. As these packets travel through the medium, the RTE is transformed into sets of ordinary differential equations along the the characteristic curve drawn by the particles. The ODEs are then solved along this characteristic curve giving the solution to the RTE. Characteristic methods perform well with problems that have complex geometries or anisotropic scattering. However, they struggle with problems that have strong absorption, where the radiation field is quickly attenuated and individual rays or packets may not be representative of the overall radiative behavior. Lastly, there is the finite element method. As the name suggests, the finite element method works by dividing the medium into some number of finite elements. Inside each of these elements, the radiative intensity is approximated using a piecewise polynomial function. Finite element methods are able to handle problems with multiple scattering, anisotropic scattering, and absorption, as well as problems with complex geometries. However, it is key that the proper mesh and polynomial order are used to achieve an accurate solution. While finer meshes and higher order polynomial functions can lead to more accurate solutions, they will also be more expensive computationally. To avoid solving the full transport equation, one of the most common approximations used is the diffusion approximation. The diffusion approximation assumes that the scattering of light is highly isotropic and that the mean free path of photons is much smaller than the characteristic length scale of the medium. The diffusion approximation is useful in situations where the medium is optically thick, meaning that the absorption coefficient is much larger than the scattering coefficient. In such cases, the radiative intensity varies slowly with position, and the diffusion equation provides a good approximation to the true transport equation. To derive the diffusion equation, the first step is to integrate the radiative transport equation over all angles and frequen-

cies.

$$\frac{\partial E_r}{\partial t} + \nabla \cdot \mathbf{F_r} + \sigma_a c E_r = \int_\nu \int_{4\pi} j_\nu d\Omega d\nu \tag{2.3.2}$$

In the equation above, $E_r$ is the radiation energy density. It is related to the specific intensity when the specific intensity is integrated over all angles and frequencies. The $\mathbf{F_r}$ term is the radiative flux which is related to the $\Omega \cdot \nabla I_\nu$ term when integrated over all angles and frequencies. The transport of radiation can be described by Fick's law, which is a well-known equation in physics that describes the diffusion of particles from areas of high concentrations to areas of low concentration. In the context of radiative transport, Fick's law states that the radiative flux is proportional to the gradient of the radiation energy density:

$$\mathbf{F_r} = -D \nabla E_r \tag{2.3.3}$$

where $\mathbf{F_r}$ is the radiative flux, $E_r$ is the radiation energy density, and $D$ is the diffusion coefficient which is found by $D = c/3\sigma_a$ where $\sigma_a$ is the material absorptivity. The radiative flux in equation 2.3.2 can be expressed using Fick's law, the emission in terms of the material temperature, and assume Local Thermal Equilibrium (LTE) to get the final form of the diffusion equation.

$$\frac{\partial E_r}{\partial t} = \nabla \cdot (D \nabla E_r) + ac\sigma T_m^4 - \sigma c E_r \tag{2.3.4}$$

For an initial implementation, this work will use the diffusion approximation as shown in equation 2.3.4 to solve for the radiation energy density. The problems explored later will be optically thick problems where the diffusion approximation will be accurate.

## 2.4 Boundary Conditions

Boundary conditions are used to constraint or impose requirements on a mathematical or physical system at its boundaries. An easy example of boundary conditions is to think of a vibrating string with length $L$. This system will require two boundary con-

ditions at the points $x = 0$ and $x = L$. At these points, boundary conditions can be prescribed such that the velocity of the string at the boundaries must be zero, an external force is applied to the string at one boundary, etc. The idea is the same when solving the hydrodynamics equations and the radiative transport equations. At the edges of the computational domain ($x = 0$ and $x = L$), two sets of boundary conditions will be needed. The first set prescribe what happens to the fluid at the boundary, and the second set prescribe what happens to the radiation at the boundary. There are a number of different boundary conditions that can be used when solving these equations. For the hydrodynamics solution, the boundary conditions are important because they can greatly effect the flow of the fluid within the domain. There are three common boundary conditions: the Dirichlet, Neumann, and mixed boundary conditions. The Dirichlet boundary condition, or first type boundary condition, is named after Peter Gustav Lejeune Dirichlet. This boundary condition works by specifying the values of the fluid variables at the boundary of the fluid domain. For example, when a fluid flows past a solid surface boundary, the velocity of the fluid at the surface might be set to be zero. The Neumann boundary condition, or second type boundary condition, is named after Carl Neumann. Neumann boundary specifies the rate of change of the fluid variables at the boundary. One example is heat transfer from a fluid to a solid surface at the boundary. This can be set proportionally to the temperature gradient at the surface. Lastly, there are mixed boundary conditions. As the name suggests, mixed boundary conditions combine the Neumann and Dirichlet boundary conditions. These are used in cases in which the velocity of a fluid may be specified at the boundary while the pressure may be allowed to vary with time or position. Hydrodynamics boundary conditions and computational fluid dynamics are explained in great detail by Versteeg and Malalasekera [22].

There are also specialized boundary conditions which can be applied to specific problems and scenarios. For example, boundary conditions that define the position and

shape of the fluid surface for free surface problems. There are also boundary conditions that define turbulence at boundaries when studying the affect of turbulence on flow. The values of the fluid flowing into and out of the boundaries can also be specified. This method is referred to as inflow and outflow boundary conditions, and is the method used in the solution of the hydrodynamics equations in this report. When considering a flow which is moving from left to right, at the left boundary the conserved variable equal is set to some "far" upstream value. At the right boundary, the conserved variable is set equal to some "far" downstream value. For the problems used to test these methods, the hydrodynamics' conserved values return to equilibrium before they reach the boundary. This allows the inflow and outflow boundary values to be set equal to the cell immediately to the right and left of their respective boundaries.

The radiative transfer equations require a different set of boundary conditions in order to be numerically solved. Like computational fluid dynamics, numerical solutions and their boundary conditions have been studied and documented extensively in literature. A few of the most common boundary conditions include vacuum boundaries, reflective boundaries, and external source boundaries. The vacuum boundary condition assumes that no radiation enters the problem from outside of the computational domain. This boundary condition works due to the mean free path of photons, neutrons, and other forms of radiation in air is much larger than of the material that they are interacting. Since this mean free path is so large, it can be said that the probability of radiation scattering back into the system is essentially zero and, as such, no radiation enters the problem from outside of the computational domain. Another function of the vacuum boundary condition is the extrapolation length which is denoted with $d$. This is the point outside the boundary of the problem that the flux goes to zero, and is calculated by $d = 2/3\lambda_{tr}$. This can be expressed mathematically as shown by equation 2.4.1.

$$\left.\frac{\partial \phi}{\partial x}\right|_d = 0 \tag{2.4.1}$$

The reflective boundary condition is essentially the opposite of the vacuum boundary condition. When radiation reaches the boundaries of the problem it is reflected back into the material so it can, in the case of photons, deposit more energy in the material. This is the boundary condition used for the radiative shock problems. Since these problems are steady state at the boundary, the reflective boundary condition can be used without causing any increase in energy deposited into the material. Lastly, there are external source boundaries. These are used when there are external sources of radiation which are being set incident on one or more of the boundaries. Like the hydrodynamics boundary conditions, boundary conditions can be combined to make mixed boundary conditions. This is common when doing external source boundaries where one surface may have some external source, and the other surfaces may be reflected or vacuum boundaries.

## 2.5 Operator Splitting

Operator splitting is a popular method for solving initial value problems that contain multiple physics, or problems in which some of the physics must be treated in an implicit fashion. When solving the radiation hydrodynamics equations, operator splitting is a popular procedure due to the characteristic differences in the time scales of the problems [6]. This is due to the photons moving at the speed of light, which is orders of magnitude faster than that of the fluid, and generally requires an implicit method to solve the radiative transport equation. The idea of operator splitting is simple and straightforward. The method starts by splitting the problem into two parts, referenced as $A$ and $B$. When solving the radiation hydrodynamics equations, the hydrodynamics solution is often process $A$, and radiative transport solutions $B$. For each time step taken, the physical process $A$ is progressed as if it was the only event taking place during that time step. After solving for process $A$, that solution is used as the starting place for process $B$. Process $B$ is then progressed as if it was the only event taking

place during the time step [6]. This can be shown using a system of equations in which some vector of conserved quantities are solved for which is referred to as $\mathbf{X}$.

$$\frac{d\mathbf{X}}{dt} = A[\mathbf{X}] + B[\mathbf{X}] \tag{2.5.1}$$

The normal solution to an equation of this form is to discretize it either explicitly as shown by equation 2.5.2 or implicitly which is shown by equation 2.5.3.

$$\frac{\mathbf{X}^{n+1} - \mathbf{X}^n}{\Delta t} = A[\mathbf{X}^n] + B[\mathbf{X}^n] \tag{2.5.2}$$

$$\frac{\mathbf{X}^{n+1} - \mathbf{X}^n}{\Delta t} = A[\mathbf{X}^{n+1}] + B[\mathbf{X}^{n+1}] \tag{2.5.3}$$

When discretized explicitly, the equations are straightforward to solve due since no information later than time $t^n$ is needed. The known values at $t^n$ can be substituted into the equation and solved for directly. However, the implicit method is much harder and computationally more expensive to solve. One method for solving these non-linear functions is as follows:

1. Set up a system of nonlinear equations for all of the unknowns $\mathbf{X}^{n+1}$.

2. Apply the Newton-Raphson method for multi-variables to the equations, and take the initial guesses of $\mathbf{X}^{n+1}$ to be $\mathbf{X}^n$.

3. For each time step, the Jacobian matrix elements are calculated, and the next set of corrections for $\mathbf{X}^{n+1}$ is solved by direct elimination.

However, Jacobian matrix elements come at a large computational cost. Due to this cost, it is preferred to not use the implicit method for physics that is not stiff and does not require it, such as the hydrodynamics solution. This is the point at which the operator splitting procedure takes place. The time derivative of the conserved value $\mathbf{X}$ can be split into k pieces, such that there will be k number of partial time steps from time

$t^n$ to $T^{n+1}$. For two processes where one processes is solved explicitly and the other implicitly, it takes the following form.

$$\begin{aligned} \frac{\mathbf{X}^{n+1/k} - \mathbf{X}^n}{\Delta t} &= A[\mathbf{X}^n] \\ \frac{\mathbf{X}^{n+2/k} - \mathbf{X}^{n+1/k}}{\Delta t} &= B[\mathbf{X}^{n+2/k}] \end{aligned} \tag{2.5.4}$$

Summing processes $A$ and $B$, and given that process $B$ is $k = 2$, the final equation for the conserved quantity using implicit-explicit operator splitting is given by:

$$\frac{\mathbf{X}^{n+1} - \mathbf{X}^n}{\Delta t} = A[\mathbf{X}^n] + B[\mathbf{X}^{n+1}] \tag{2.5.5}$$

While this method allows the stiff radiative transfer to be solved implicitly and the non-stiff hydrodynamics equations explicitly, a large disadvantage of this approach is that it is only first order accurate as presented. If there are only two operators ($A$ and $B$) the accuracy can be improved by the Strang splitting method [6]. This form of splitting alternates the order in which the operators are executed with each time step. Other high order methods for IMEX operator splitting, such as self-consistent implicit-explicit (IMEX) methods and IMEX Runge-Kutta methods, have been developed by Samet et. al [11] and Ascher et. al [4].

# 3 Numerical Implementation

As discussed in Section 2.5, an operating splitting procedure to solve the hydrodynamics equations explicitly while solving the radiation part implicitly. This is necessary due to the stiff radiation diffusion equation caused by the absorption and emission terms $\sigma c E_r$ and $\sigma a c T^4$ respectively. The operator splitting procedure goes as follows:

*1. Hydrodynamics Solve Step*

*2. Radiation Material Motion Correction (MMC)*

*3. Radiation Solve Step*

*4. Energy Deposition Step*

where the hydrodynamics solve step and radiation material motion correction are solved explicitly, and the radiation solve step and energy deposition step are solved implicitly.

## 3.1 Fixed Mesh Eulerian

In the Eulerian frame, the operator split equations take the following form

*1. Hydrodynamics Solve Step*

$$\frac{\rho_i^{n+1} - \rho_i^n}{\Delta t} = -\frac{(\rho u)_{i+1/2}^n - (\rho u)_{i-1/2}^n}{\Delta x} \tag{3.1.1}$$

$$\frac{\rho_i^{n+1} u_i^{n+1} - \rho_i^n u_i^n}{\Delta t} = -\frac{(\rho uu + P)_{i+1/2}^n - (\rho uu + P)_{i-1/2}^n}{\Delta x} \tag{3.1.2}$$

$$\begin{aligned}\frac{\rho_i^{n+1} E_{h,i}^{n+1} - \rho_i^n E_{h,i}^n}{\Delta t} = &-\frac{(\rho E_h u + Pu)_{i+1/2}^n - (\rho E_h u + Pu)_{i-1/2}^n}{\Delta x} \\ &+ P_r^n \left( \frac{u_{i+1/2}^n - u_{i-1/2}^n}{\Delta x} \right)\end{aligned} \tag{3.1.3}$$

$$e_{h,i}^{n+1} = E_{h,i}^{n+1} - (0.5 u_i^{n+1})^2 \tag{3.1.4}$$

$$T_i^h = \frac{e_{h,i}^{n+1}}{c_{v,i}} \tag{3.1.5}$$

*2. Radiation MMC Step*

$$\frac{E_{r,i}^* - E_{r,i}^n}{\Delta t} = -\frac{(E_r u)_{i+1/2}^n - (E_r u)_{i-1/2}^n}{\Delta x} - P_r^n \left( \frac{u_{i+1/2}^n - u_{i-1/2}^n}{\Delta x} \right) \tag{3.1.6}$$

*3. Radiation Solve Step*

$$\frac{E_{r,i}^{n+1} - E_{r,i}^*}{\Delta t} = -\frac{F_{r,i+1/2}^{n+1} - F_{r,i-1/2}^{n+1}}{\Delta x} - \sigma c E_{r,i}^{n+1} + ac\sigma (T_i^4)^{n+1} \tag{3.1.7}$$

$$F_{r,i-1/2}^{n+1} \approx -D_{i-1/2} \frac{E_i^{n+1} - E_{i-1}^{n+1}}{\Delta x} \quad F_{r,i+1/2}^{n+1} \approx -D_{i+1/2} \frac{E_{i+1}^{n+1} - E_i^{n+1}}{\Delta x} \tag{3.1.8}$$

$$\frac{T^{n+1} - T^h}{\Delta t} = \frac{\sigma c E_r^{n+1} - ac\sigma(T^4)^{n+1}}{\rho C_v} \tag{3.1.9}$$

*4. Energy Deposition Step*

$$E_i^{n+1} = E_{h,i}^{n+1} + c_v(T^{n+1} - T^h) \tag{3.1.10}$$

In the above equations, values with the subscript $h$ denote the hydrodynamics quantities, and values with the subscript $r$ denote the radiation quantities. The term $e_h$ represents the internal hydrodynamics energy, and $T^h$ represents the hydrodynamics temperature.

## 3.2 Moving Mesh Eulerian

Using operator splitting and applying the formula for the moving mesh gives the following equations. However, there is now an extra step of calculating the mesh velocity, new node positions, and the new cell volumes. This step takes place in three location when using the moving mesh method. The first is during the problem initialization. Next is after the predictor step of the predictor corrector method where the predicted mesh velocity, location, and cell volumes are calculated. Lastly, at the end of the time step when the conserved values are re-assigned, the mesh velocity, location, and cell volumes are also re-assigned. These values can be calculated using equations 3.2.1, 3.2.2, and 3.2.3.

$$w_{i-1/2}^{n+1} = \frac{z_{i-1}^n u_{i-1}^n + z_i^n u_i^n - (P_i^n - P_{i-1}^n)}{z_i^n + z_{i-1}^n} \tag{3.2.1}$$

$$x_{i-1/2}^{n+1} = x_{i-1/2}^n + \Delta t w_{i-1/2}^{n+1} \tag{3.2.2}$$

$$V_i^{n+1} = x_{i+1}^{n+1} - x_i^{n+1} \tag{3.2.3}$$

*1. Hydro Solve Step*

$$\frac{1}{V_i^n}\frac{(\rho V)^{n+1} - (\rho V)^n}{\Delta t} = -\frac{(\rho(u-w))_{i+1/2}^n - (\rho(u-w))_{i-1/2}^n}{V_i^n} \tag{3.2.4}$$

$$\frac{1}{V_i^n}\frac{(\rho u V)^{n+1}-(\rho u V)^n}{\Delta t} = -\frac{(\rho u(u-w)+P)^n_{i+1/2}-(\rho u(u-w)+P)^n_{i-1/2}}{V_i^n} \tag{3.2.5}$$

$$\frac{1}{V^n}\frac{(\rho E_h V)^{n+1}-(\rho E_h V)^n}{\Delta t} = -\nabla\cdot[(\rho^n E_h^n(u-w)^n + P^n u^n)] + p_r^n \nabla\cdot u^n \tag{3.2.6}$$

$$e_{h,i}^{n+1} = E_{h,i}^{n+1} - (0.5u_i^{n+1})^2 \tag{3.2.7}$$

$$T_i^h = \frac{e_{h,i}^{n+1}}{c_{v,i}} \tag{3.2.8}$$

*2. Radiation MMC Step*

$$\begin{aligned}\frac{1}{V_i^n}\frac{E_r^* V^{n+1}-E_r^n V^n}{\Delta t} = &-\frac{(E_r(u-w))^n_{i+1/2}-(E_r(u-w))^n_{i-1/2}}{V_i^n} \\ &-P_r^n\left(\frac{u^n_{i+1/2}-u^n_{i-1/2}}{V_i^n}\right)\end{aligned} \tag{3.2.9}$$

*3. Radiation Solve Step*

$$\frac{E_{r,i}^{n+1}-E_{r,i}^*}{\Delta t} = -\frac{F_{i+1/2}^{n+1}-F_{i-1/2}^{n+1}}{\Delta x_i} - \sigma c E_i^{n+1} + ac\sigma(T_i^4)^{n+1} \tag{3.2.10}$$

$$F_{i-1/2}^{n+1} \approx -D_{i-1/2}\frac{E_i^{n+1}-E_{i-1}^{n+1}}{\Delta x_{i-1/2}} \quad F_{i+1/2}^{n+1} \approx -D_{i+1/2}\frac{E_{i+1}^{n+1}-E_i^{n+1}}{\Delta x_{i+1/2}} \tag{3.2.11}$$

$$\frac{T^{n+1}-T^h}{\Delta t} = \frac{\sigma c E_r^{n+1} - ac\sigma(T^4)^{n+1}}{\rho C_v} \tag{3.2.12}$$

*4. Energy Deposition Step*

$$E_i^{n+1} = E_{h,i}^{n+1} + c_v(T^{n+1}-T^h) \tag{3.2.13}$$

## 3.3 Second Order Hydrodynamics Solutions

Although the IMEX method used is not second order preserving, the hydrodynamics solutions are solved for using second order methods in time and space. This allows for better shock resolution and stability in the presence of discontinuities or large gradients. This is done using a predictor-corrector method for the second order in time solu-

tion, and a MUSCL scheme for the second order in space solution.

### 3.3.1 Predictor Corrector

In order to achieve second order accuracy in time for the hydrodynamic solution, the predictor corrector method was used. As has been discussed, the overall radiation-hydrodynamics solution is not second order due to the IMEX splitting. However, second order methods are used for the hydrodynamics solutions. The predictor corrector method works in two steps. The first, or "predictor" step, works by extrapolating a polynomial fit to the derivative from the previous points to a new point. Given this value, the second, or "corrector" step, interpolates the derivative to get the value at the new point [23]. This is shown by equations 3.3.1 and 3.3.2.

*Predictor*

$$y^{n+1/2} = y^n + \frac{\Delta t}{2} f(y^n) \tag{3.3.1}$$

*Corrector*

$$y^{n+1} = y^n + \Delta t f(y^{n+1/2}) \tag{3.3.2}$$

### 3.3.2 MUSCL Scheme

The MUSCL scheme is used to calculate the hydrodynamics flux, $F_{i+1/2}$ and $F_{i-1/2}$, in equation 3.3.3.

$$U_i^{n+1} = U_i^n + \Delta t \left( \frac{F_{i+1/2} - F_{i-1/2}}{\Delta x} \right) \tag{3.3.3}$$

The term MUSCL stands for Monotone Upstream-centered Schemes for Conservation Laws [21]. It was developed to provide high accuracy numerical solutions to partial differential equations which can involve solutions that exhibit shocks, discontinuities, or large gradients. The method works by replacing the piecewise constant approximations in the Gudonov scheme. This is done by using reconstructive states which are derived from cell-averaged states obtained from the previous time-step. The reconstructed left

and right states, which are flux limited, are obtained and used to calculate the fluxes at the cell boundaries. These fluxes are then used as an input for the Reimann solver from which the solutions are averaged and used to advance the solution in time [13]. The first step of the MUSCL scheme is to find the extrapolated cell edge variables $u_{i\pm1/2}$.

$$\begin{aligned} U^L_{i+1/2} = U_i + 0.5\phi(r_i)(U_{i+1} - U_i) \;\; U^R_{i+1/2} = U_{i+1} - 0.5\phi(r_{i+1})(U_{i+2} - U_{i+1}) \\ U^L_{i-1/2} = U_{i-1} + 0.5\phi(r_{i-1})(U_i - U_{i-1}) \;\; U^R_{i-1/2} = U_i - 0.5\phi(r_i)(U_{i+1} - U_i) \end{aligned} \tag{3.3.4}$$

When solving this numerically, the cell edges, or nodes, are looped over, allowing for just the first and third terms in equation 3.3.4 to be solved.

$$U^L_{i+1/2} = U_i + 0.5\phi(r_i)(U_{i+1} - U_i) \;\; U^L_{i-1/2} = U_{i-1} + 0.5\phi(r_{i-1})(U_i - U_{i-1}) \tag{3.3.5}$$

In these equations $\phi(r_i)$ represents the flux limiter. The flux limiter helps to prevent oscillations that might occur due to shocks or discontinuities. There are many choices for flux limiters; however, this report will look at the Van Leer limiter.

$$\phi(r_i) = \frac{r + |r|}{1 + |r|} \tag{3.3.6}$$

where

$$r_i = \frac{u_i - u_{i-1}}{u_{i+1} - u_i} \tag{3.3.7}$$

The flux values can be calculated once the reconstructed left and right quantities have been obtained. This process again loops over the nodes to get the values of $F^{L,R}_{i-1/2}$.

$$F^L = F(u^L) \;\; F^R = F(u^R) \tag{3.3.8}$$

After finding the left and right flux values, the Rusanov approximate Riemann solver is

used to get the numerical fluxes at the cell boundaries.

$$F^{Rusanov} = 0.5(F_L + F_R) - 0.5S^*(U_R - U_L) \tag{3.3.9}$$

$S^*$ is the interface signal velocity can be found by

$$S^* = max(|q_L| + a_L, |q_R| + a_R) \tag{3.3.10}$$

where q is the face normal component of the velocity. e.g.,

$$q = \vec{u} \cdot \hat{n} \tag{3.3.11}$$

Once the Rusanov flux has been found for the left and right faces $i \pm 1/2$ they can be substituted into equation 3.3.3.

### 3.4 Radiation Energy Density and Material Temperature Solver

When solved explicitly, the radiation energy density and material temperature equations can be very unstable if a sufficiently small time step is not taken. However, this time step for stability is often prohibitively small as the computation time becomes impractically large. To overcome this, the radiation energy density and material temperature are solved implicitly. This allows the use of larger time steps without sacrificing stability of the numerical solutions. The implicit solve does requires two iterative loops, the inner loop solves for the material temperature using the Newton iterative method, and the outer loop will solve for the radiation energy using a tri-diagonal matrix.

### 3.4.1 Material Temperature

The inner loop to solve for the material temperature starts by guessing a value that approximates the values of $E^{n+1}$ and $T^{n+1}$ which will be denoted as $E^k$ and $T^k$. With these guesses, the residual function can be calculated for the material temperature.

$$\mathcal{R}_T(E_i^k, T_i^k) = \rho C_v \frac{T_i^k - T_i^n}{\Delta t} - \sigma_i c E_i^k + \sigma a c (T_i^k)^4 \tag{3.4.1}$$

Over this inner loop the value of $E^k$ is treated as a constant allowing for only the change in material temperature $\delta T_i^k$ to be determined.

$$\frac{\partial \mathcal{R}_T}{\partial T_i^k} \delta T_i^k = -\mathcal{R}_T(E_i^k, T_i^k) \tag{3.4.2}$$

The first step is to take the derivative of the material residual function with respect to $T_i^k$.

$$\frac{\partial \mathcal{R}_T}{\delta T_i^k} = \frac{\rho C_v}{\Delta t} + 4ac\sigma_i (T_i^k)^3 \tag{3.4.3}$$

After taking the derivative, the change in material temperature $\delta T_i^k$ can be solved for. This change in material temperature is then added to the initial guess $T^k$ which gives the initial guess for the next iteration.

$$T_i^{k+1} = T_i^k + \delta T_i^k \tag{3.4.4}$$

This iteration is performed until the value of $\delta T_i^k \leq 10^{-3}$. At this value the change in the temperature at $k+1$ is insignificant.

### 3.4.2 Radiation Energy Density

This discussion of solving for the radiation energy density will use the fixed mesh Eulerian method as an example. The fixed mesh method will always have a uniform mesh

which allows the diffusion terms to have a simplified form when compared to a non-uniform mesh. The equations on a non-uniform mesh can be found in appendix A. The solution starts by substituting equation 3.2.11 into equation 3.2.10, and grouping the radiation energy density terms based on cell index.

$$\left(\frac{1}{\Delta t}+\frac{D_{i+1/2}}{\Delta x^2}+\frac{D_{i-1/2}}{\Delta x^2}+\sigma_i c\right)E_i^{n+1}-\frac{D_{i+1/2}}{\Delta x^2}E_{i+1}^{n+1}-\frac{D_{i-1/2}}{\Delta x^2}E_{i-1}^{n+1} = ac\sigma(T_i^4)^{n+1}+\frac{E_i^n}{\Delta t} \tag{3.4.5}$$

To keep from storing the whole matrix, which would be mostly zeros, only the three matrix diagonals from the $E_{i-1}$ , $E_i$ , and $E_{i+1}$ terms, as well as the right hand side of the equation are stored. The lower ($E_{i-1}$), middle ($E_i$), and upper ($E_{i+1}$) rows of the matrix ared denoted using $a$, $b$, and $c$ respectively, and the right hand side of the equation with $d$.

$$a_i=-\frac{D_{i-1/2}}{\Delta x^2} \tag{3.4.6}$$

$$b_i=\left(\frac{1}{\Delta t}+\frac{D_{i+1/2}}{\Delta x^2}+\frac{D_{i-1/2}}{\Delta x^2}+\sigma_i c\right) \tag{3.4.7}$$

$$c_i=-\frac{D_{i+1/2}}{\Delta x^2} \tag{3.4.8}$$

$$d_i=\sigma ac(T_i^k)^4+\frac{E_i^n}{\Delta t} \tag{3.4.9}$$

Once the diagonals and the right hand side of the equation have been stored, the radiation energy density terms are solved for using a Tridiagonal matrix algorithm also known as a Thomas Algorithm. This method is based on LU decomposition and allows the matrix $MX = r$ to be expressed in terms of the lower and upper triangle matrices such that $MX = r$ becomes $LUx = r$. This system can be solved for by setting $Ux = \rho$ and solving $L\rho = r$ for $\rho$ and then $Ux = \rho$ for $x$ which is done in two steps. Step one decomposes the matrix into $M = LU$ and solves $L\rho = r$ in a single downwards sweep. This converts from $Mx = r$ to $Ux = \rho$. The second step solves the equation $Ux = \rho$

for $x$ in a single upward sweep. A detailed explanation of solving tridiagonal and band diagonal systems of equations can be found in section 2.4 of *Numerical Recipes in C* by Press [18]. An example Thomas Algorithm implementation in c++ can be seen below.

```
void Thomas_Algorithm(vector<double> &a, vector<double> &b,
                      vector<double> &c, vector<double> &r,
                      vector<double> &sol){
    \\Number of Cells
    int nx = a.size();
    \\Temporary vectors forward elimination
    std::vector<double> tmp(nx,0);
    std::vector<double> tmp2(nx,0);
    \\Forward elimination
    tmp[0] = c[0]/b[0];
    for(int i=1; i<nx-1; i++){
        tmp[i] = c[i]/(b[i]-a[i]*tmp[i-1]);
    }
    tmp2[0] = r[0]/b[0];
    for(int i=1; i<nx; i++)
    {
        tmp2[i] = (r[i]-a[i]*tmp2[i-1])/(b[i]-a[i]*tmp[i-1]);
    }
    \\Backward Substitution
    sol[nx-1] = tmp2[nx-1];
    for(int i=nx-2; i>=0; i--){
        sol[i] = tmp2[i]-tmp[i]*sol[i+1];
    }
}
```

Listing 1: c++ Thomas Algorithm Implementation

This iteration is performed until the $|E_i^{n-1} - E_i^n|$ is less than $1.0E-3$ at which point the change in energy is small enough to be insignificant.

# 4 Results

Four test problems were used to compare and verify the physics of the two methods. The first comparison is a pure test of the hydrodynamics using the Sod shock tube problem. This problem both verifies the physics of the hydrodynamics and allows for a comparison of the methods. The physics of the radiation solve step is then verified using a Marshak Wave problem. Lastly, the methods are compared with three radiative shock problems. The first two are a Mach 1.2 and Mach 3 shock where the shock is stationary, and the third is a Mach 1.2 shock with a moving shock.

## 4.1 Sod Shock Tube

The Sod shock tube problem is named after Gary A. Sod who largely researched the problem in 1978. Since the problem has an analytical solution which can be found using a Riemann Solver, it is a popular test problem for numerical hydrodynamic codes. The problem consists of a tube that is separated at the middle by a diaphragm. This tube is filled with an ideal gas at different pressures and densities on the left and right hand side of the diaphragm. A diagram of the problem can be seen in Figure 4. When

Figure 4: Sod shock tube at t=0s. Left hand side shows region of high density, pressure, and temperature.

the diaphragm bursts or is removed, the time evolution change of the problem can be modeled. From this, the propagation speed of the rarefraction wave, contact discontinuity, and shock discontinuity can be found. Since the analytical solution can be found using the Riemann Solver, the numerical implementations' ability to resolve the shocks and contact discontinuities and reproduce the correct density profile of the rarefaction

wave can be directly compared. The initial conditions for the problem can be seen below [19].

$$\begin{pmatrix} \rho_L \\ P_L \\ u_L \end{pmatrix} = \begin{pmatrix} 1.0 \\ 1.0 \\ 0 \end{pmatrix} \begin{pmatrix} \rho_R \\ P_R \\ u_R \end{pmatrix} = \begin{pmatrix} 0.125 \\ 0.1 \\ 0 \end{pmatrix}$$

A computational domain of 1.0 cm is used and the problem is run to a final time of 0.2 seconds. The fixed and moving mesh methods will be compared to the Riemann solution which is computed with the same values. The regions of the Sod Shock problem can be seen in Figure 5 below. Regions I and V show the initial condition of the problem, region II is the expansion region, region III is the contact discontinuity, and region IV is the shock.

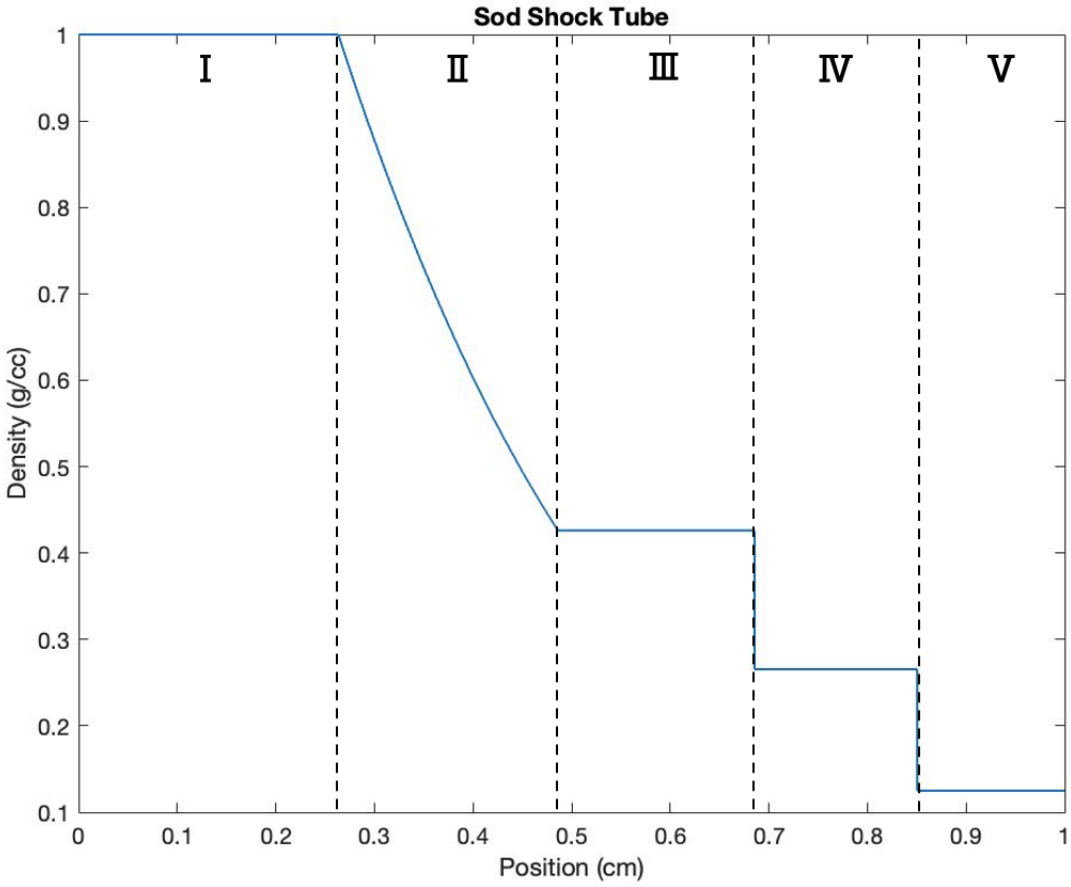


Figure 5: Regions of Sod Shock Problem at t = 0.2 seconds.

The two methods will be compared on their ability to match the analytical solution using 250, 500, 1000, and 5000 cells. By doing this, the convergence of the numerical to the analytical solution can be tracked as the mesh refines. It will also determine if the moving mesh method is able to better resolve the shock and contact discontinuity with a coarser mesh as expected.

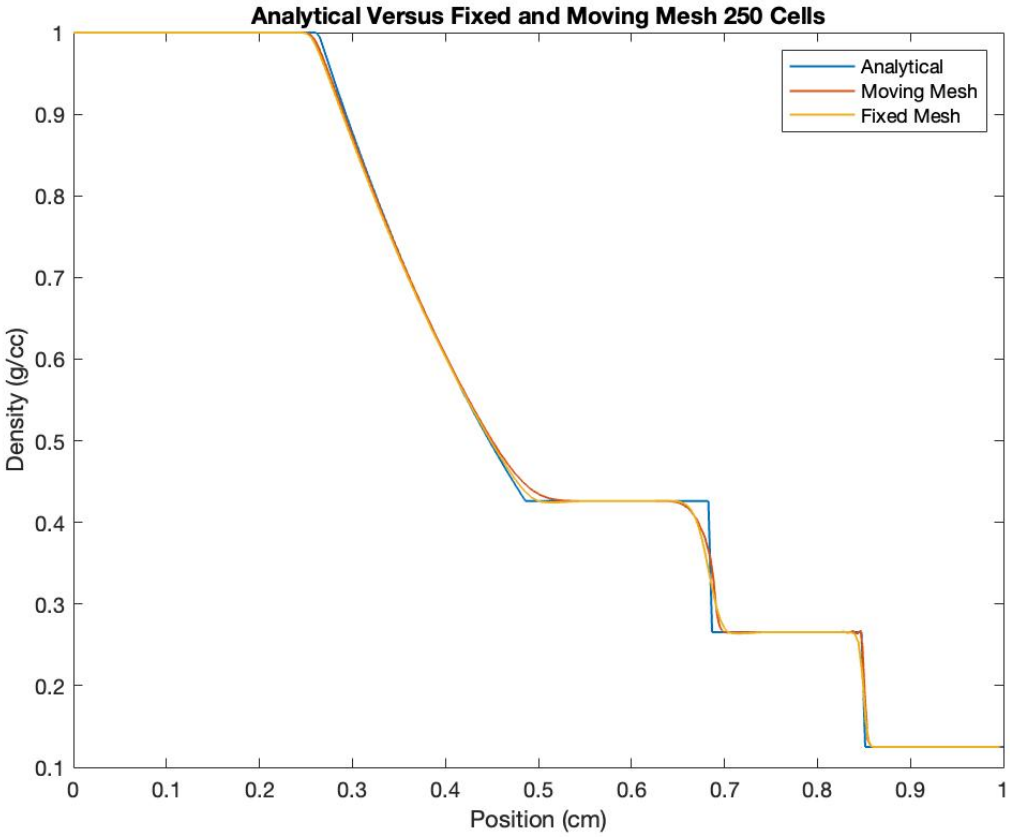


Figure 6: Sod shock tube density profile w/ 250 cells.

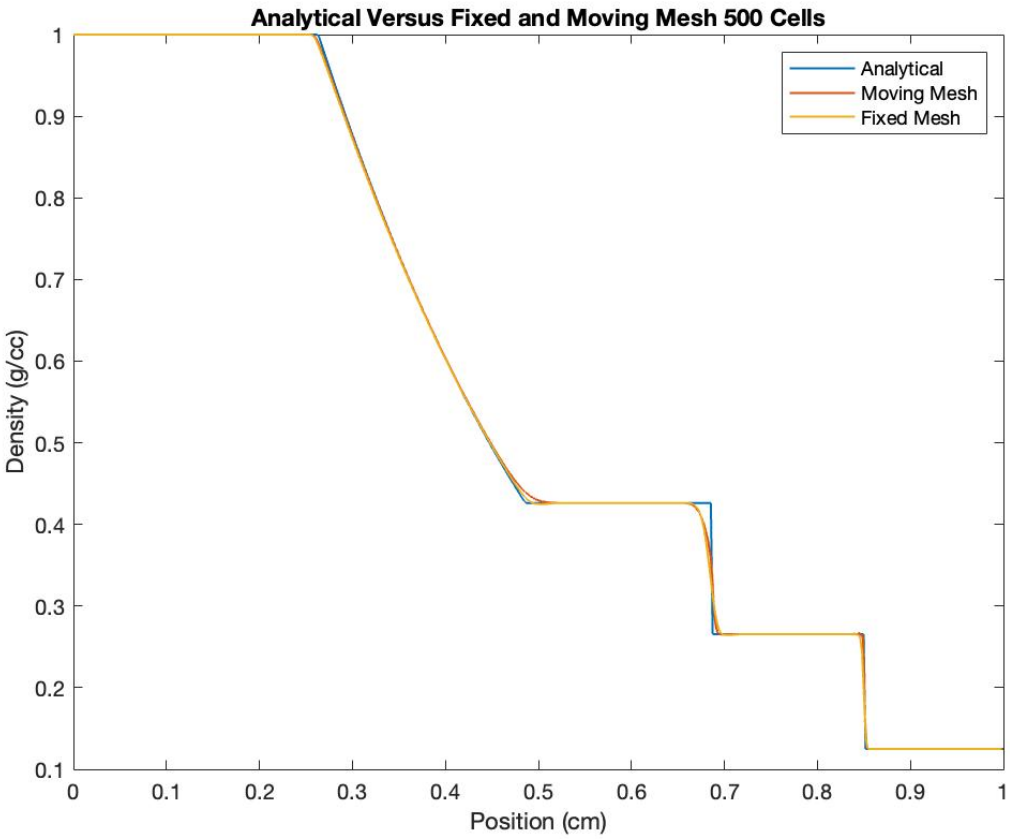


Figure 7: Sod shock tube density profile w/ 500 cells.

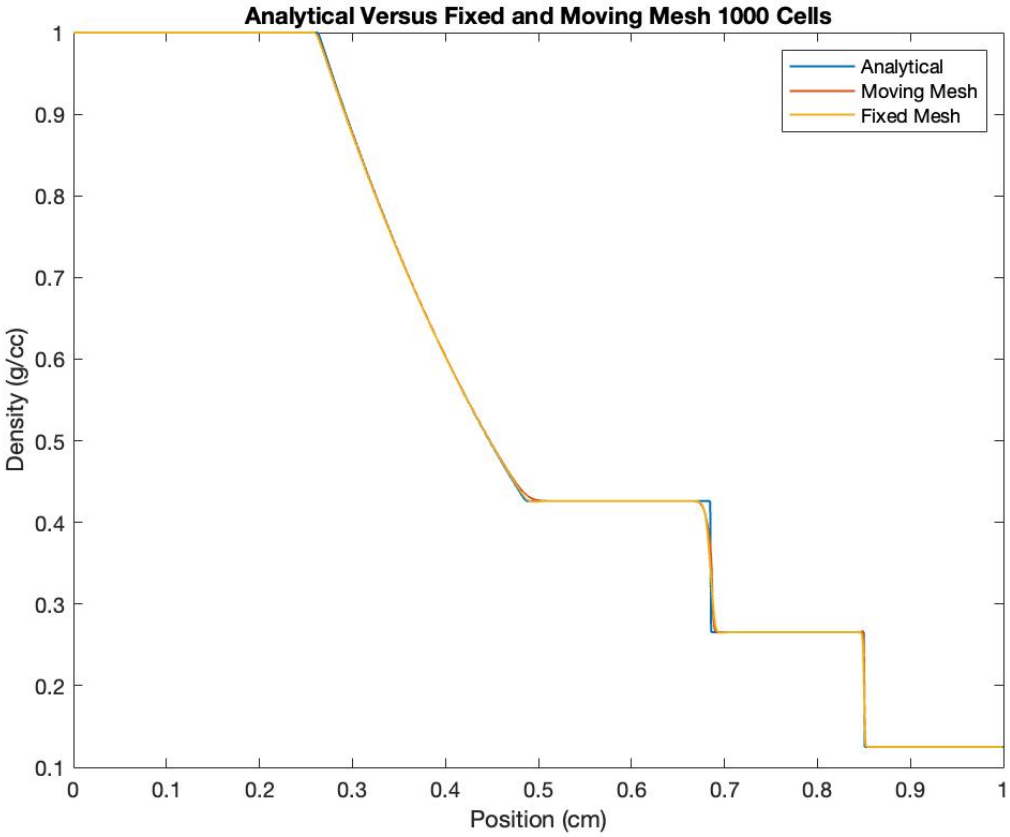


Figure 8: Sod shock tube density profile w/ 1000 cells.

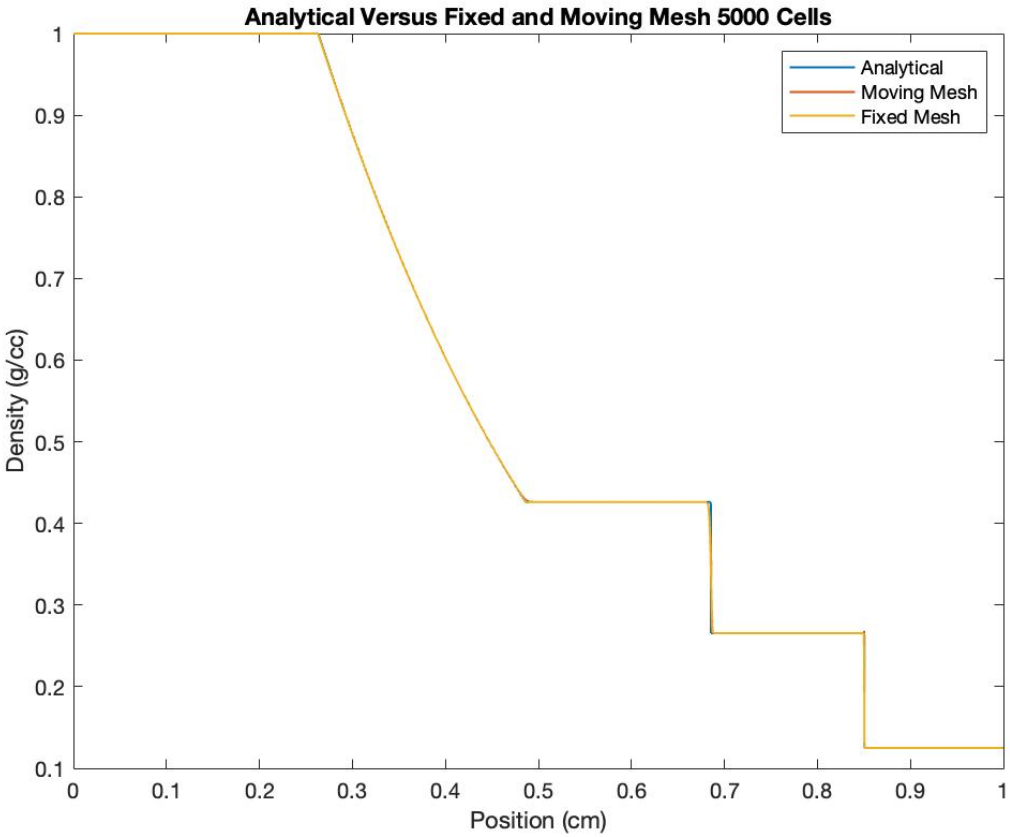


Figure 9: Sod shock tube density profile w/ 5000 cells.

In Figures 6 to 9 it can be seen that both the fixed and moving mesh methods are able to match the analytical results. However, looking at the contact discontinuity $\approx 0.7$ $cm$ and shock location $\approx 0.85$ $cm$ of the 250 and 500 cells solutions (Figures 6 and 7), the moving mesh is able to resolve the contact discontinuity and shock better than the fixed mesh. Although the difference may be small, this is expected due to the physics of this problem being very simple. As problems with steeper or non-stationary shocks are tested, the ability of the moving mesh to resolve the shock with a coarser mesh will have a larger impact on the solution.

## 4.2 Marshak Wave

Radiative heat waves, also known as Marshak Waves, play an important part in high energy density physics. During his time working in Los Alamos, New Mexico, Robert Marshak developed the explanation for how radiative heat waves propagate and interact with materials in extreme temperatures. This development resulted in them being called Markshak Waves. These are self-similar waves which can be treated with the thermal diffusion approximation. The material is classified with a constant specific heat capacity, and a mean opacity which varies as a power of the temperature. These waves have sharp fronts caused by the non-linear behavior between the material opacity and specific heat capacity [14]. The waves propagate through the material with time, but the shape of the front remains constant. The hydrodynamic motion when running this problem is ignored, and the material properties of density and specific heat capacity are set to constant values. Although this assumption is technically inaccurate, it allows for testing of just the radiative transport physics. For the moving mesh method the mesh is static, so the moving mesh method essentially just becomes a fixed mesh method. However, since there are differences in the formulation of the radiative transfer equations, it is useful to test both methods to verify the physics.
The problem geometry is a slab which is located at $x = 0$, with a width of 2 $cm$, and is set with an initial temperature of 0.025 $eV$. At $t = 0$, a 150 $eV$ radiation source is applied at $x = 0$ $cm$. The problem is assumed to be under Local Thermal Equilibrium (LTE), characterized by the radiation energy density being equal to the radiation constant times the material temperature to the fourth power ($E_r = aT_m^4$) [8]. The solution is checked at $t = 5.0 \times 10^{-8}$ seconds to see how the front has propagated through the material. The expected solution is a material and radiation temperature just less than 140 $eV$ at the left boundary, with the material temperature being slightly lower than the radiation temperature. The temperature should then decrease through the domain reaching equilibrium again at a distance of 1.5 $cm$.

| Parameter | Value | Units |
|---|---|---|
| $t_f$ | $5.0 \times 10^{-8}$ | s |
| $\Delta t$ | $1 \times 10^{-12}$ | s |
| $x_i$ | 0 | cm |
| $x_f$ | 2 | cm |
| $\Delta x$ | .025 | cm |
| $\rho$ | 1 | g/cc |
| $C_v$ | $1.3874 \times 10^{11}$ | $erg\ eV^{-1}\ g^{-1}$ |
| $\sigma$ | $10^6/T_m^3$ | $cm^{-1}$ |
| $T_{0,r}$ | 0.025 | eV |
| $T_{0,m}$ | 0.025 | eV |
| $T_{B.C.}$ | 150 | eV |

Table 1: Marshak Wave Input Parameters

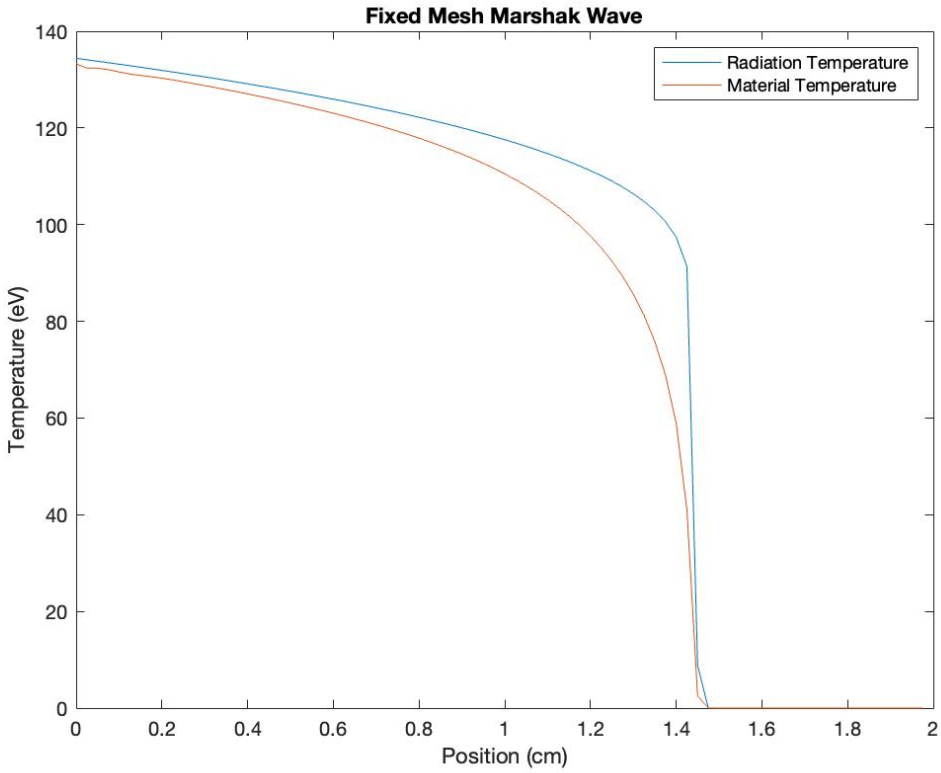


Figure 10: Marshak Wave using the fixed mesh implementation. Results match the expected physics for peak temperature and distance at which problem returns to equilibrium.

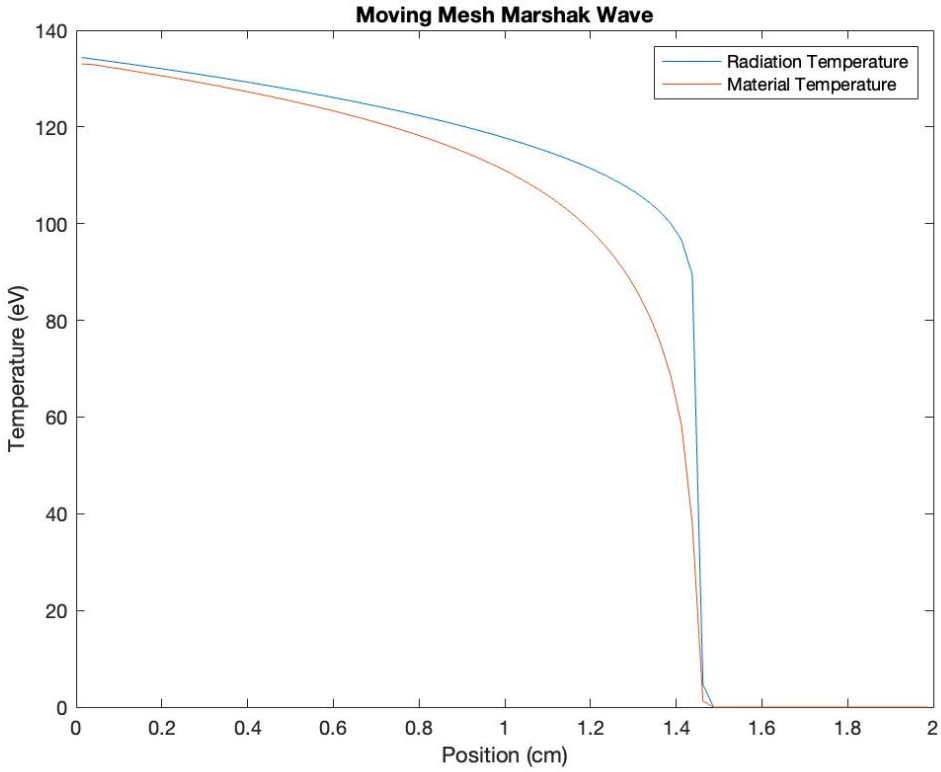


Figure 11: Marshak Wave Using the Moving Mesh Implementation. Results match the expected physics for peak temperature and distance at which problem returns to equilibrium. Gap in the left hand side of the problem is due to averaging node locations to get cell center.

### 4.3 Fixed Radiative Shocks

Due to the complexity of the coupled hydrodynamics and radiation flow, there are fewer test problems, especially those with analytical solutions, compared to hydrodynamics tests. However, radiative shock problems are one of the most studied and used for testing radiation hydrodynamics codes. These problems define strong shocks in which the material is heated to a sufficiently high temperature for the radiation and kinetic energy flux to be comparable. The shock is treated as a discontinuity and define jump relations which are used to find the equilibrium states of the far upstream and downstream material. These conditions are known as Rankine-Hugoniot jump conditions, given their name from the work done by Scottish engineer and physicist William

John Macquorn Rankine, and French engineer Pierre Henri Hugoniot. For flow moving left to right, these problems will assume that all conditions post-shock, also referred to as upstream, are known and will be referred to as region 1. The values pre-shock, also referred to as downstream, need to be determined by the jump conditions. Figure 12 shows the upstream and downstream regions of a problem with fluid flow from left to right.

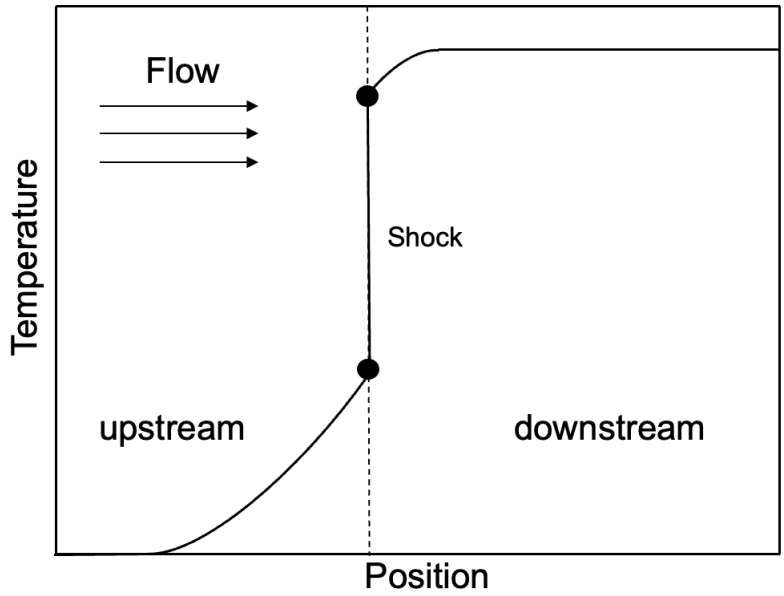


Figure 12: Upstream and downstream locations using shock as the reference point.

There is no heat added or removed from the flow as it traverses the shock waves, thus making the shock adiabatic [11]. The jump conditions can be expressed in four equations which are shown by equations 4.4.1, 4.4.2, 4.4.3, and 4.4.4.

$$S(\rho_2 - \rho_1) = \rho_2 u_2 - \rho_1 u_1 \tag{4.3.1}$$

$$S(\rho_2 u_2 - \rho_1 u_1) = (\rho_2 u_2^2 + P_2) - (\rho_1 u_1^2 + P_1) \tag{4.3.2}$$

$$S(\rho_2 E_{h,2} - \rho_1 E_{h,1}) = (\rho_2 E_{h,2} u_2 + P_2 u_2) - (\rho_1 E_{h,1} u_1 + P_1 u_1) \tag{4.3.3}$$

$$S(\rho_2 E_{r,2} - \rho_1 E_{r,1}) = (\rho_2 E_{r,2} u_2) - (\rho_1 E_{r,1} u_1) \tag{4.3.4}$$

Assuming a calorically perfect gas allows the use of thermodynamic relationships to solve for the material pressure

$$P_1 = \rho_1 R T_1 \tag{4.3.5}$$

where R denotes the gas constant, $\rho_1$ is the density in region 1, and $T_1$ is the temperature in region 1. The gas constant can be expressed in many units but the value used in this report is $R = 9.6492284 \times 10^{11}\ erg\ eV^{-1}\ mol^{-1}$. The fluid velocity is found as a function of the Mach number of the shock and the sound speed in the material using equation 4.3.6.

$$u_1 = \frac{M_1}{a_{s1}} \tag{4.3.6}$$

This equation comes from the definition of the Mach speed, the ratio of the velocity of the fluid to the sound speed of the fluid ($M = \frac{u}{a_s}$). The Mach number is used to characterize how fast an object is moving relative to the speed of sound ahead of the shock wave. When the Mach number is less than one ($M < 1$), the fluid is traveling slower than the speed of sound and the shock is considered to be weak. When the opposite is true, with a Mach number greater than one ($M > 1$), the fluid is moving faster than the speed of sound and the shock is considered to be strong. Once the density, pressure, and velocity in region 1 have been determined, the total hydro energy can then be found.

$$E_h = c_v \rho T + 0.5 \rho u^2 \tag{4.3.7}$$

In the jump condition equations 4.4.1, 4.4.2, 4.4.3, and 4.4.4, the term $S$ is used to denote the shock propagation speed. For a standing shock, the shock propagation speed is set to be zero ($S = 0$). For a stationary shock, the pressure and density jump condition equations take the form as shown in equations 4.3.8 and 4.3.9. A detailed derivation of these equations can be found in [3].

$$\frac{P_2}{P_1} = 1 + \frac{2\gamma}{\gamma + 1}(M_1^2 - 1) \tag{4.3.8}$$

$$\frac{\rho_2}{\rho_1} = \frac{u_2}{u_1} = \frac{(\gamma+1)M_1^2}{2+(\gamma-1)M_1^2} \tag{4.3.9}$$

Two standing shock problems will be used to compare the methods. The first test has a Mach number of 1.2, and the second test is a stronger shock with a Mach number of 3. For both problems the shock will be located at the center of the problem domain. When plotting the material temperatures, there are three regions of the plots that are of interest. The first is the precursor region in which the temperature will increase from the equilibrium value towards the shock. The second region is the shock itself. The last region is the relaxation region in which the values return to their post-shock equilibrium values. The relaxation region will be more prevalent in the Mach 3.0 problem that contains a Zel'dovich spike. The Zel'dovich spike is a phenomenon caused by the maximum temperature being greater than the equilibrium temperature of region 1. This occurs due to sudden cooling of the gas behind the shock front. As the radiative shock wave moves through a medium, it heats the gas to very high temperatures causing it to emit intense radiation. However, as the gas behind the shock wave cools, the radiation it emits becomes less intense. This, as a result, causes a rapid drop in the radiation temperature, which results in a sharp increase in the radiation pressure. The spike forms because the shock front slows down as it encounters the high radiation pressure, creating a region of high pressure and density immediately behind the shock front. The precursor, shock, Zel'dovich spike, and relaxation regions can be seen in Figure 13.

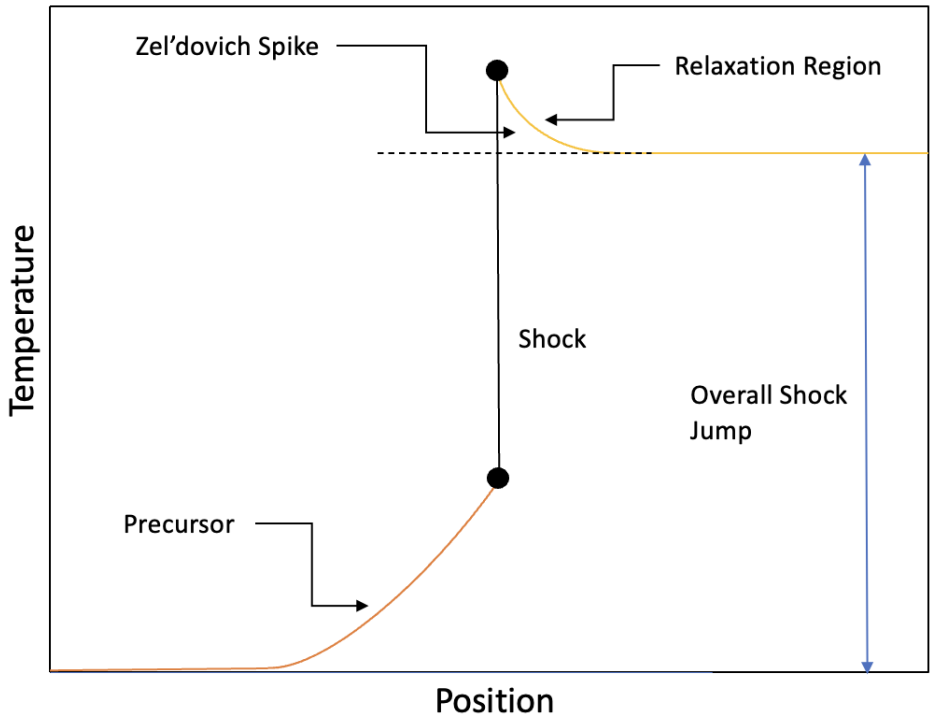


Figure 13: Precursor, shock, relaxation, and Zel'dovich spike regions of radiative shock problems with fixed shocks.

Both problems use $\gamma = 5/3$, $c_v = 1.4467 \times 10^{12}$ erg $ev^{-1}$ $g^{-1}$, and $\sigma_a = \sigma_t = 577.35$ $cm^{-1}$. The problems run to a final time of 5 ns at which point the problem reaches steady state using a time step of $1.0 \times 10^{-12}s$. The upstream and downstream values for both problems can be seen in Tables 2 and 3.

| Parameter | upstream | downstream | Units |
|---|---|---|---|
| $\rho$ | 1.0000000 | 1.29731782 | g/cc |
| u | $1.52172533 \times 10^7$ | $1.17297805 \times 10^7$ | cm/s |
| T | 100 | 119.475741 | eV |
| E | $2.60510396 \times 10^{14}$ | $3.13573034 \times 10^{14}$ | erg/cc |

Table 2: upstream and downstream initial values for the Mach 1.2 radiative shock problem.

| Parameter | upstream | downstream | Units |
|---|---|---|---|
| $\rho$ | 1.0000000 | 3.00185103 | g/cc |
| u | $3.80431331 \times 10^7$ | $1.26732249 \times 10^7$ | cm/s |
| T | 100 | 366.260705 | eV |
| E | $8.68367987 \times 10^{14}$ | $1.83229115 \times 10^{15}$ | erg/cc |

Table 3: Upstream and downstream initial values for the Mach 3.0 radiative shock problem.

Since there is a not an analytical solution for the Mach 1.2 and Mach 3 problems, a very fine mesh composed of 15,000 cells is used as a reference solution. The ability of the methods to resolve the shock and, in the case of the Mach 3 problem, the Zel'dovich spike with 500, 1000, 2000, and 4000 cells will be tracked. To make the results easier to read, the material and radiation temperatures will be presented separately. The first results presented will be for the Mach 1.2 problem.

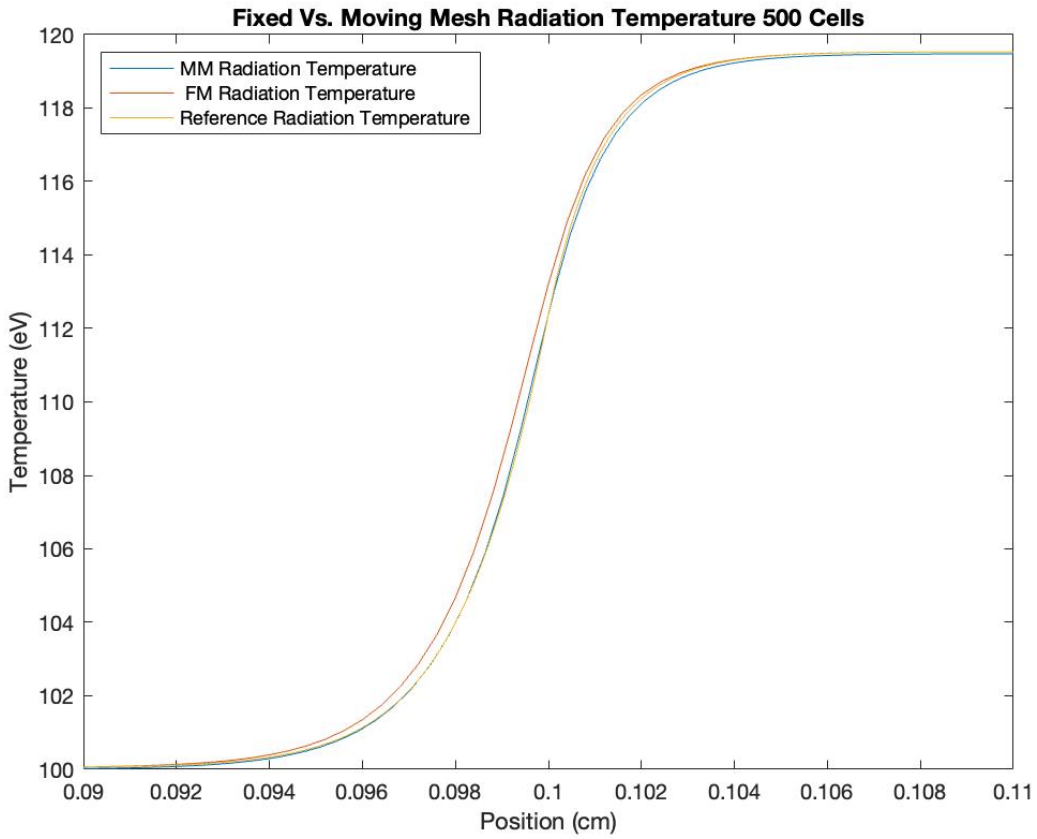


Figure 14: Radiation temperature for Mach 1.2 shock w/ 500 cells.

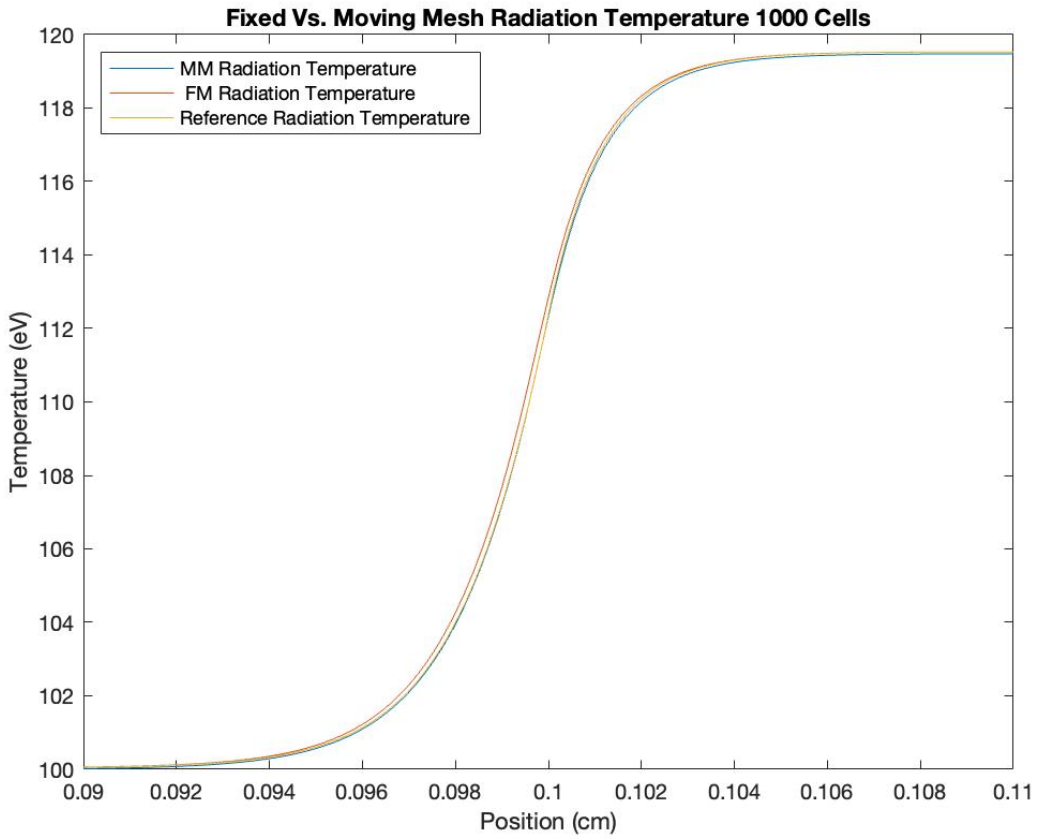


Figure 15: Radiation temperature for Mach 1.2 shock w/ 1000 cells.

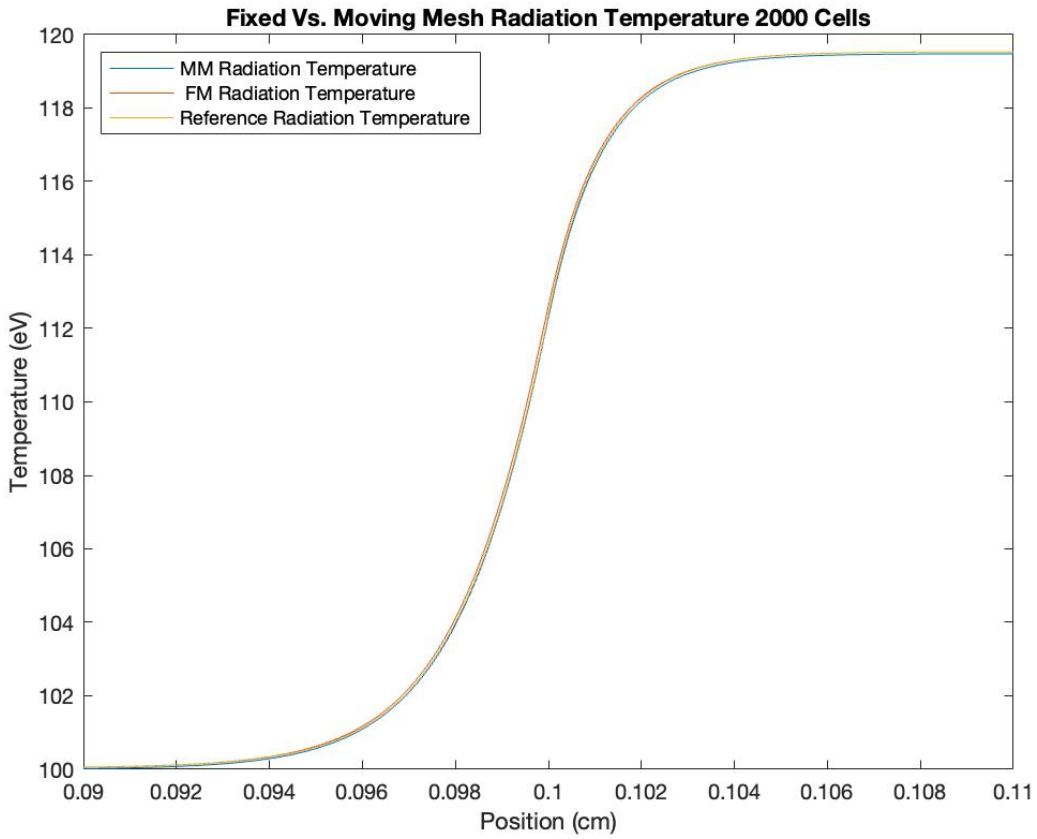


Figure 16: Radiation temperature for Mach 1.2 shock w/ 2000 cells.

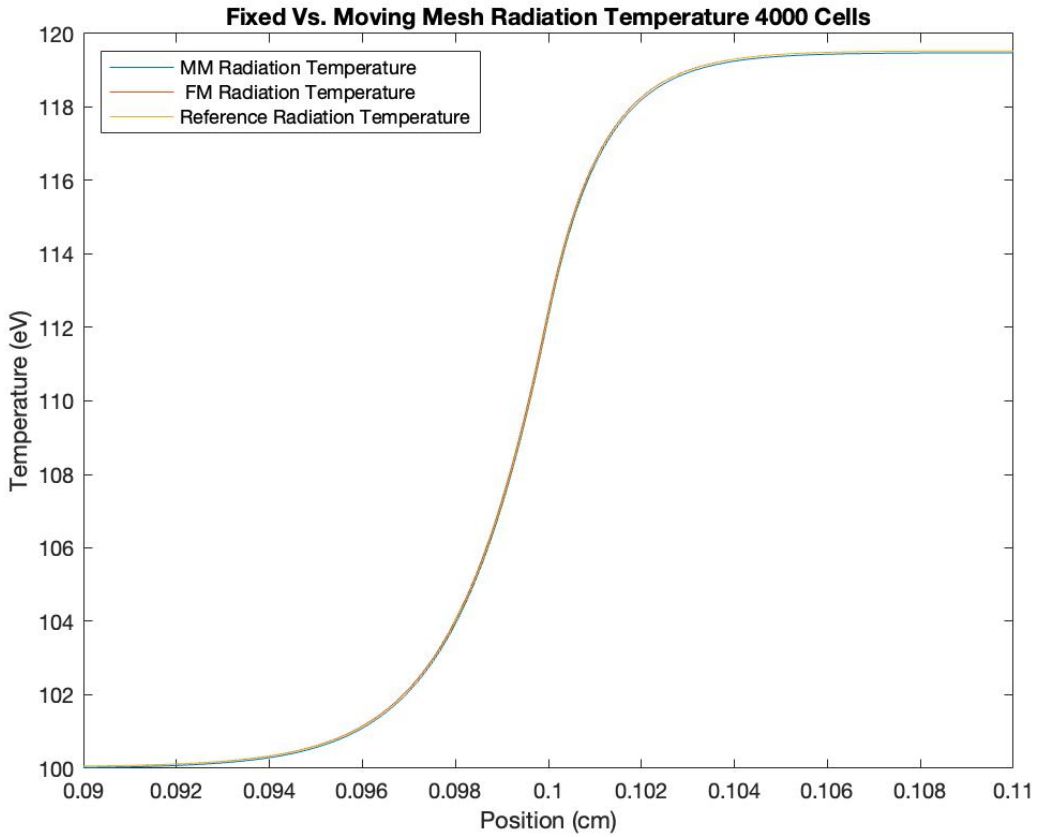


Figure 17: Radiation temperature for Mach 1.2 shock w/ 4000 cells.

On fine meshes of 2000 and 4000 cells both methods are able to match the reference solution for the radiation temperature very well. However, with just 500 cells, the moving mesh solution is able to match the reference solution with much higher accuracy than the fixed mesh solution. The difference in the methods is most visible in the region spanning from 0.094 cm to 0.10 cm. In this region, the fixed mesh solution is slightly diffused to the left from the reference solution, but the moving mesh case is able to almost perfectly match the reference solution. This is repeated with the 1000 cells solution. However, the fixed mesh case is much closer to the reference solution of the radiation temperature.

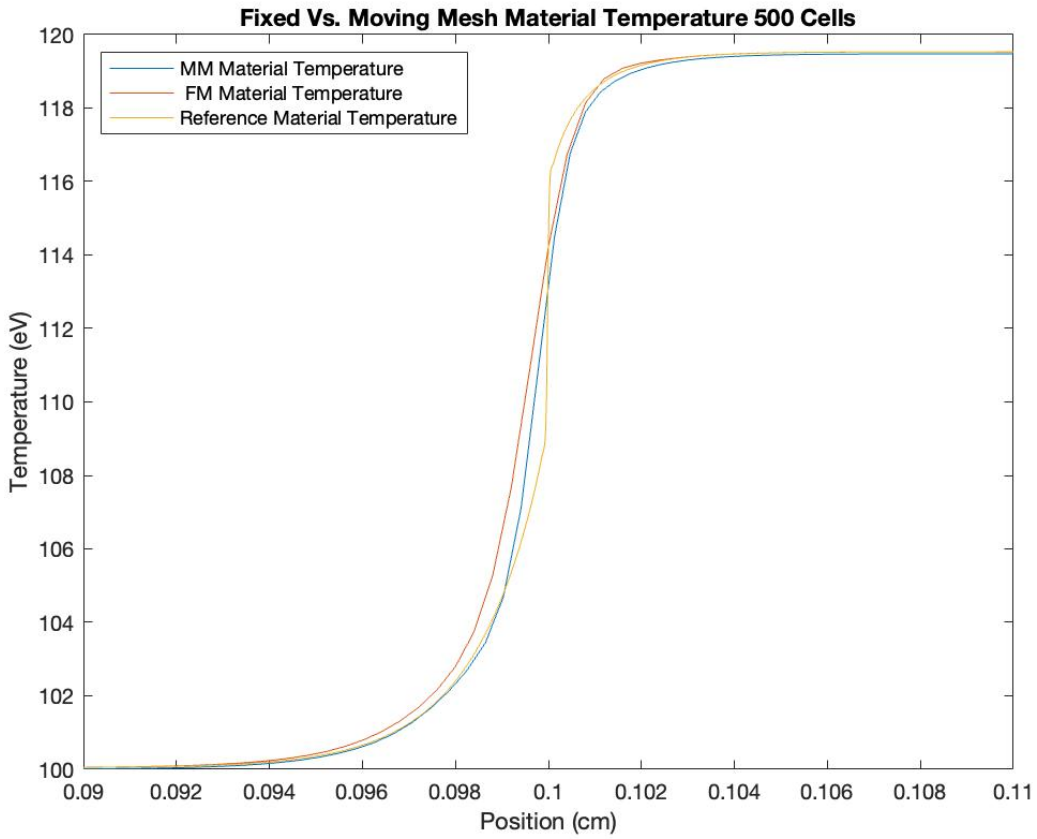


Figure 18: Material temperature for Mach 1.2 shock w/ 500 cells.

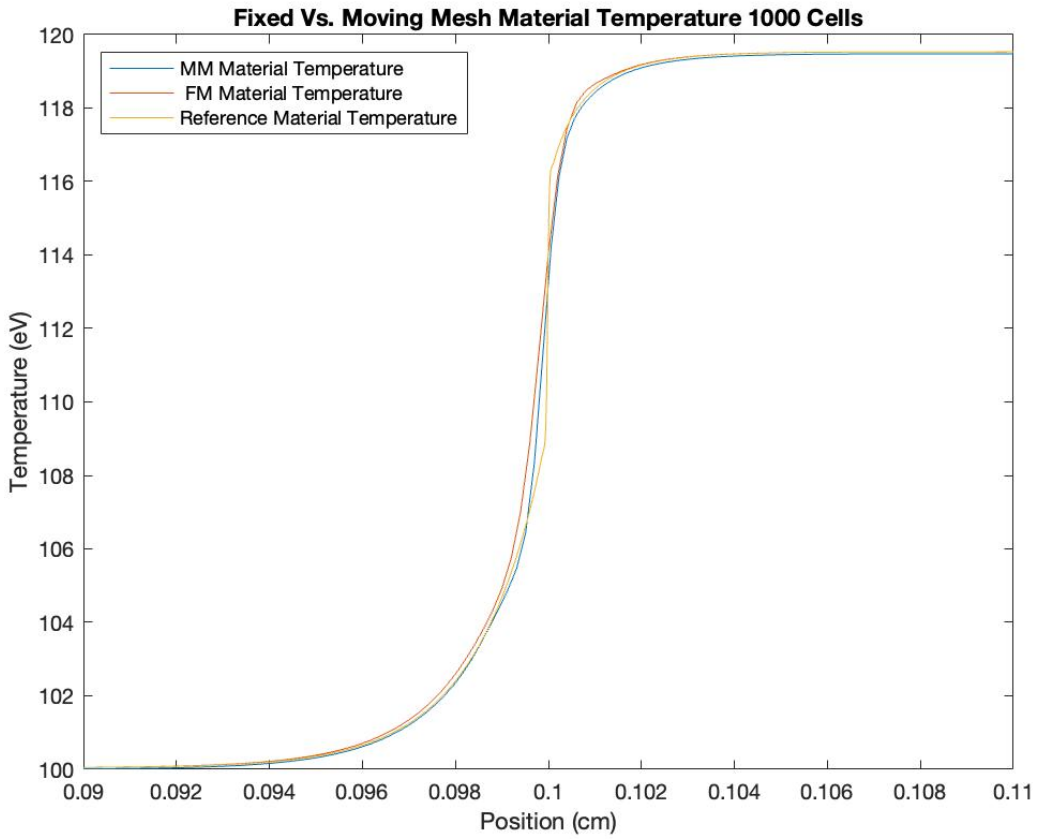


Figure 19: Material temperature for Mach 1.2 shock w/ 1000 cells.

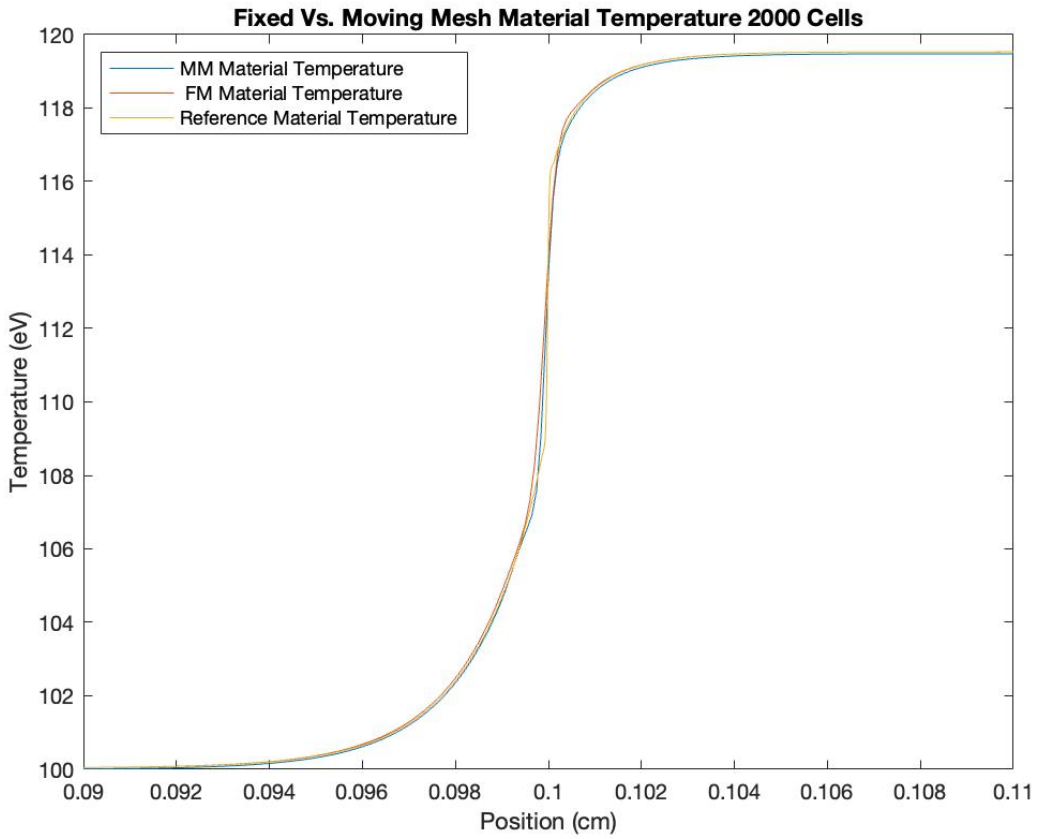


Figure 20: Material temperature for Mach 1.2 shock w/ 2000 cells.

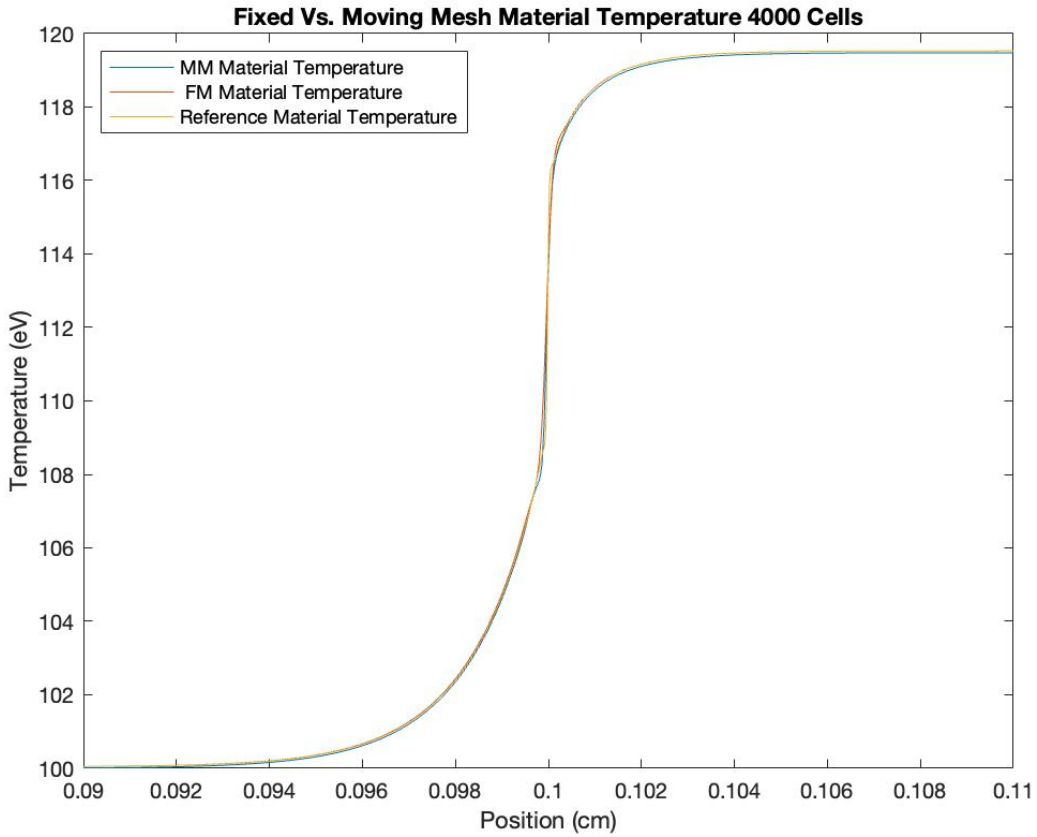


Figure 21: Material temperature for Mach 1.2 shock w/ 4000 cells.

Due to the presence of the shock in the material temperature, getting accurate results that match the reference solution with coarse grids, such as the 500 and 1000 cell cases, is difficult for both the fixed and moving mesh implementations. However, in looking at the results of the 500 cell case, specifically at the precursor region leading into the shock, it can still be seen that the moving mesh case is able to better match the reference solution in this region. As with the radiation temperature, as the mesh is refined, both methods are able to match the reference solution with more accuracy.

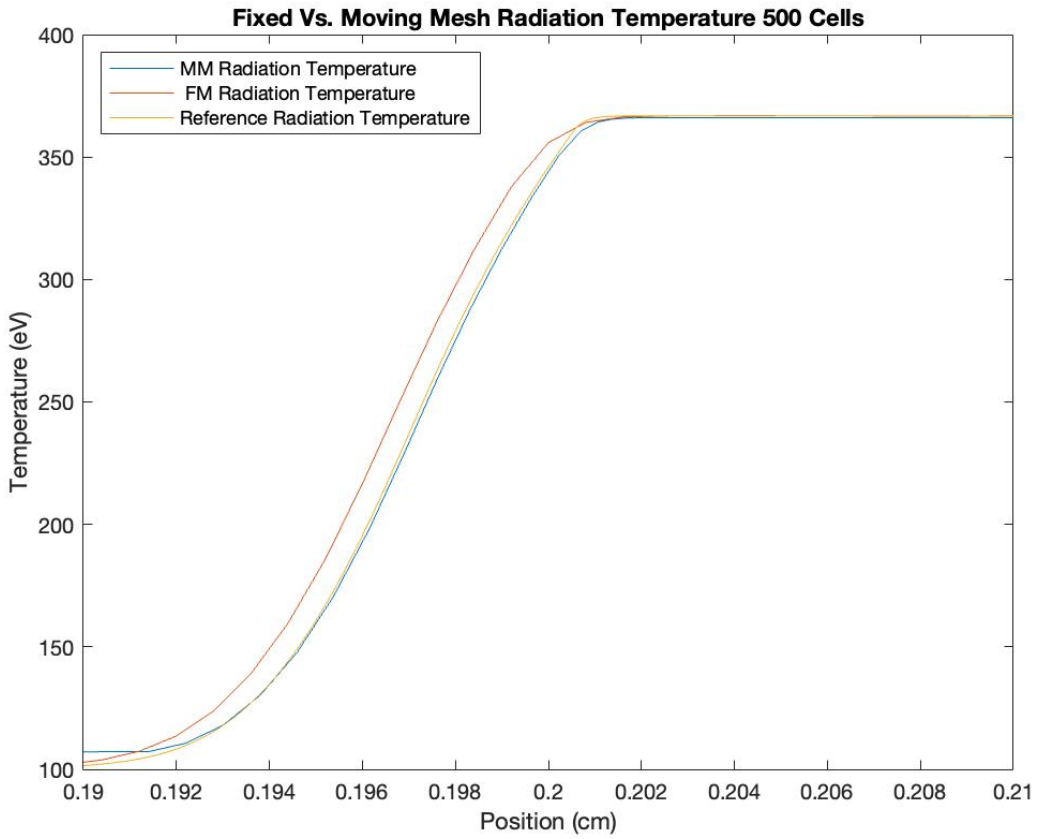


Figure 22: Radiation temperature for Mach 3.0 shock w/ 500 cells.

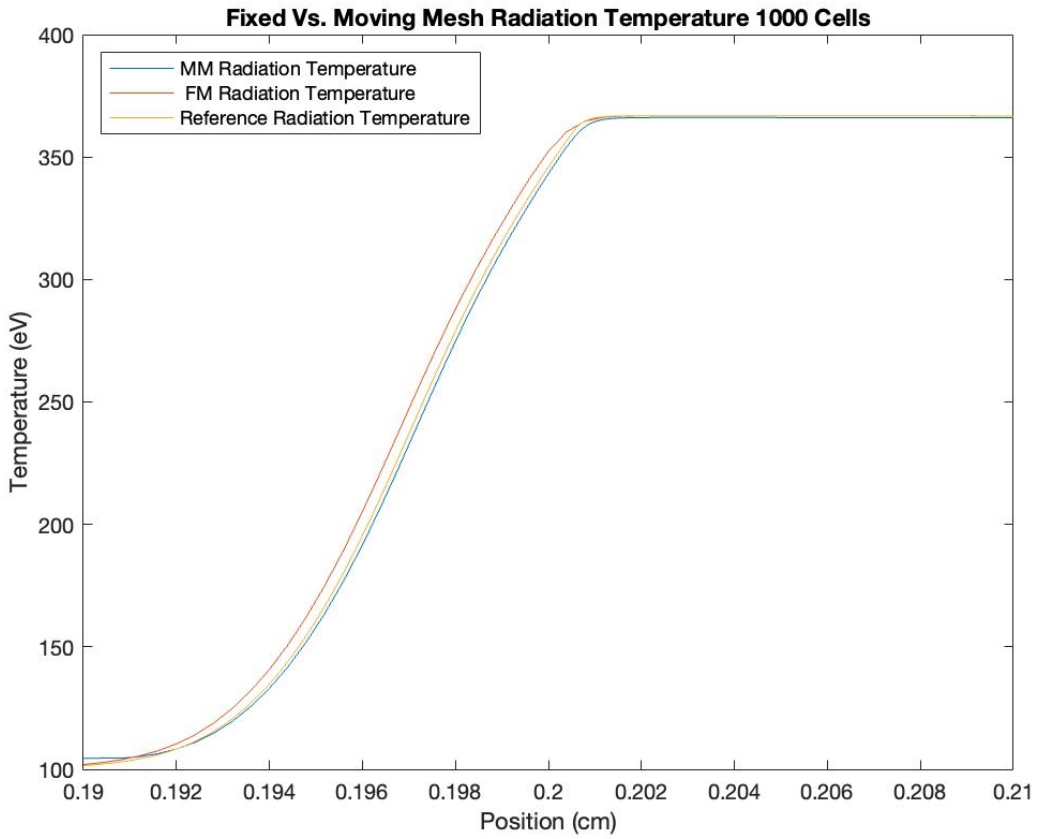


Figure 23: Radiation temperature for Mach 3.0 shock w/ 1000 cells.

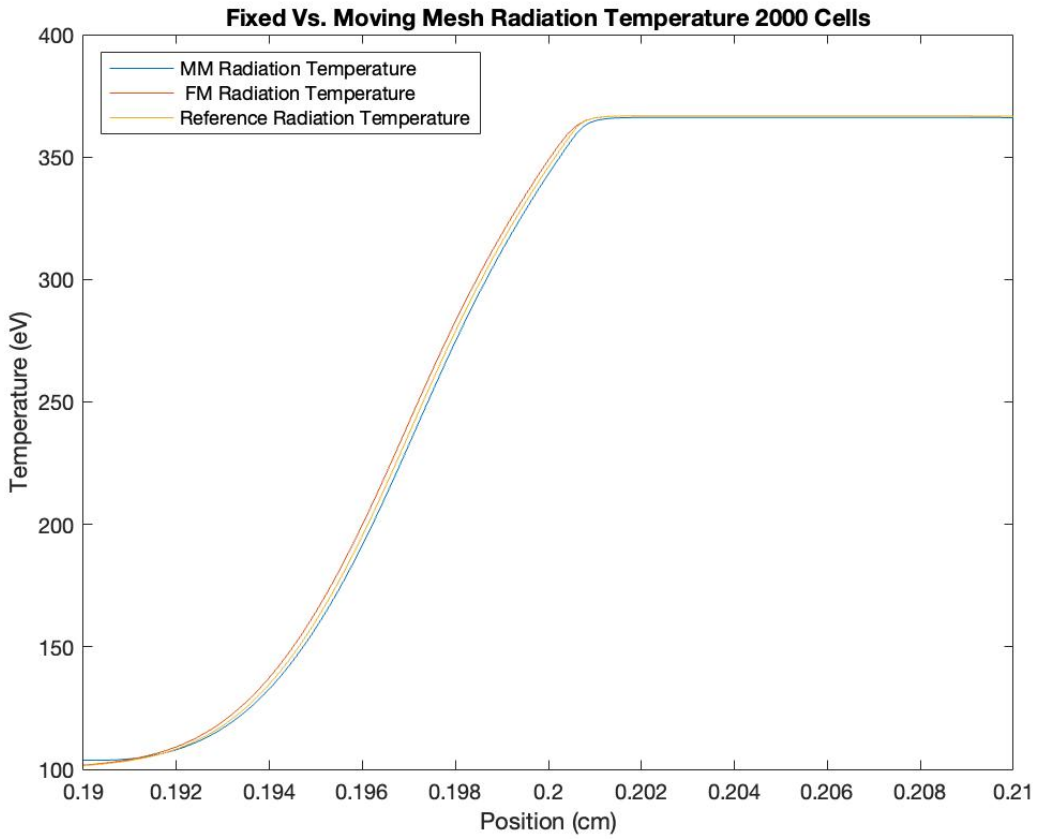


Figure 24: Radiation temperature for Mach 3.0 shock w/ 2000 cells.

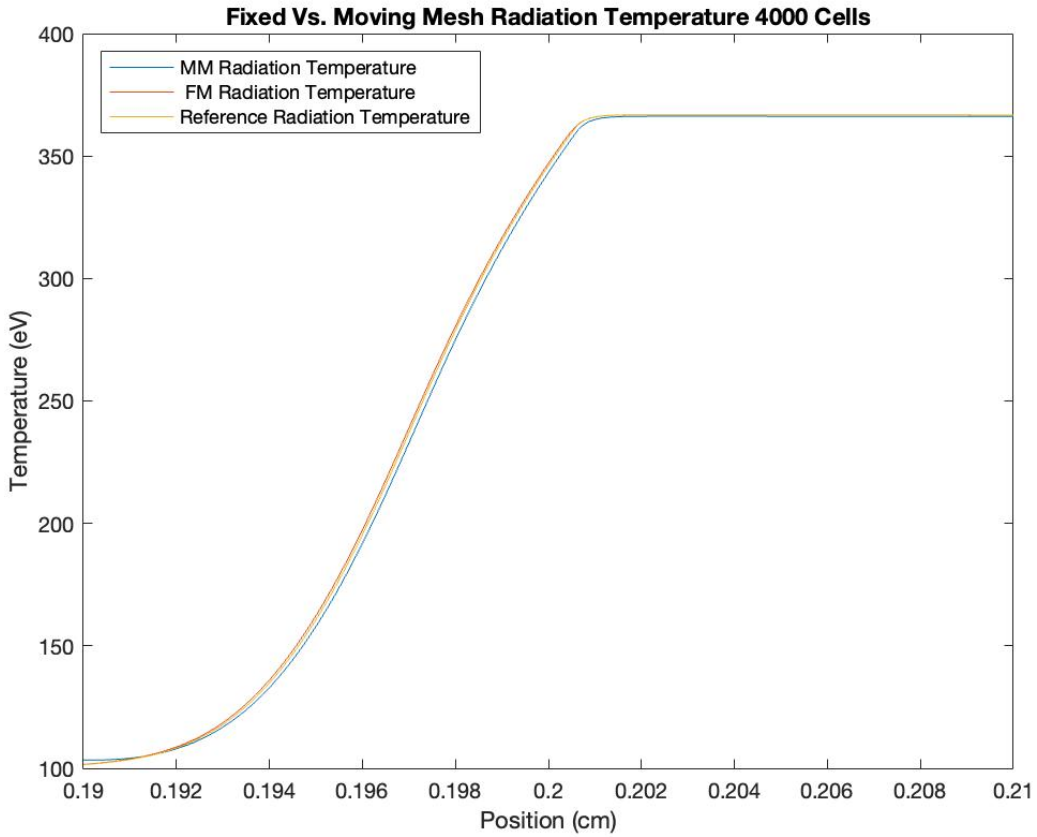


Figure 25: Radiation temperature for Mach 3.0 shock w/ 4000 cells.

As with the Mach 1.2 problem, the moving mesh case is again able to achieve better agreement with the reference solution utilizing a coarser mesh for the radiation temperature. The fixed mesh case also requires more cells in order to match the convergence to the reference solution when compared to the Mach 1.2 problem. For the Mach 3 problem, the fixed mesh solution doesn't match the moving mesh solution of 500 cells until the finest mesh of 4000 cells. The scale of this difference is more noticeable when compared to the Mach 1.2 problem. In the Mach 1.2 problem, agreement in the results of the fixed and moving mesh case could be seen with just 1000 cells.

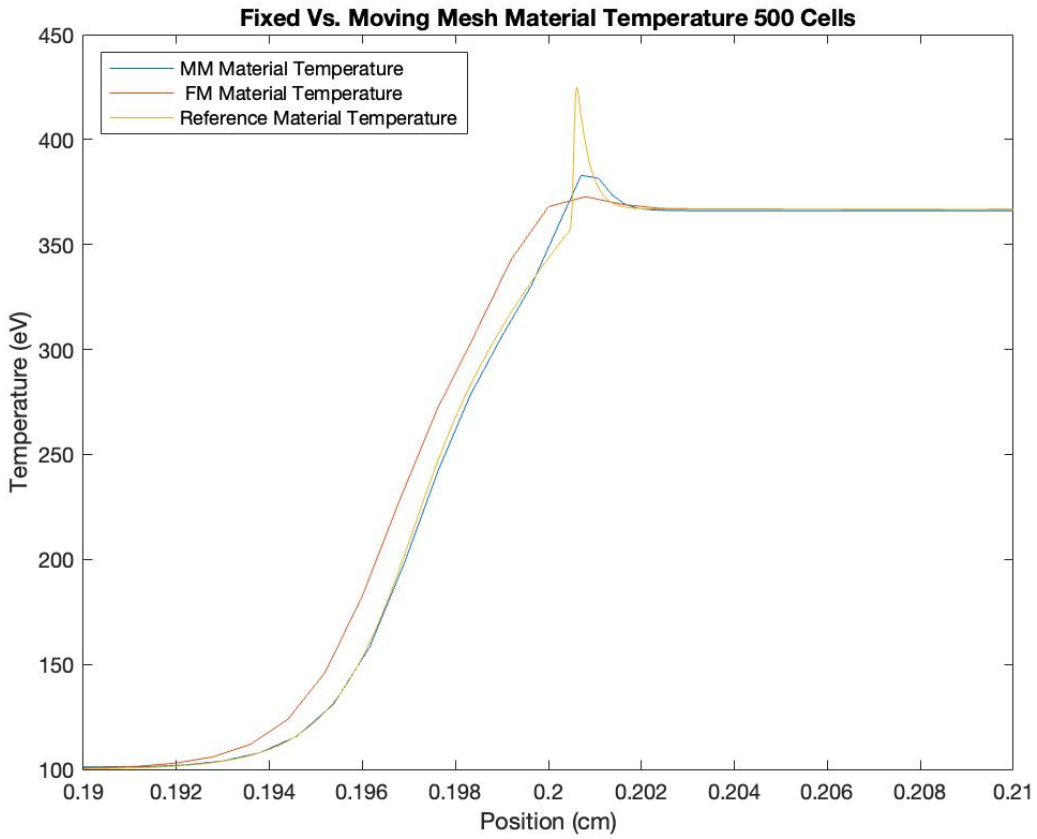


Figure 26: Material temperature for Mach 3.0 shock w/ 500 cells.

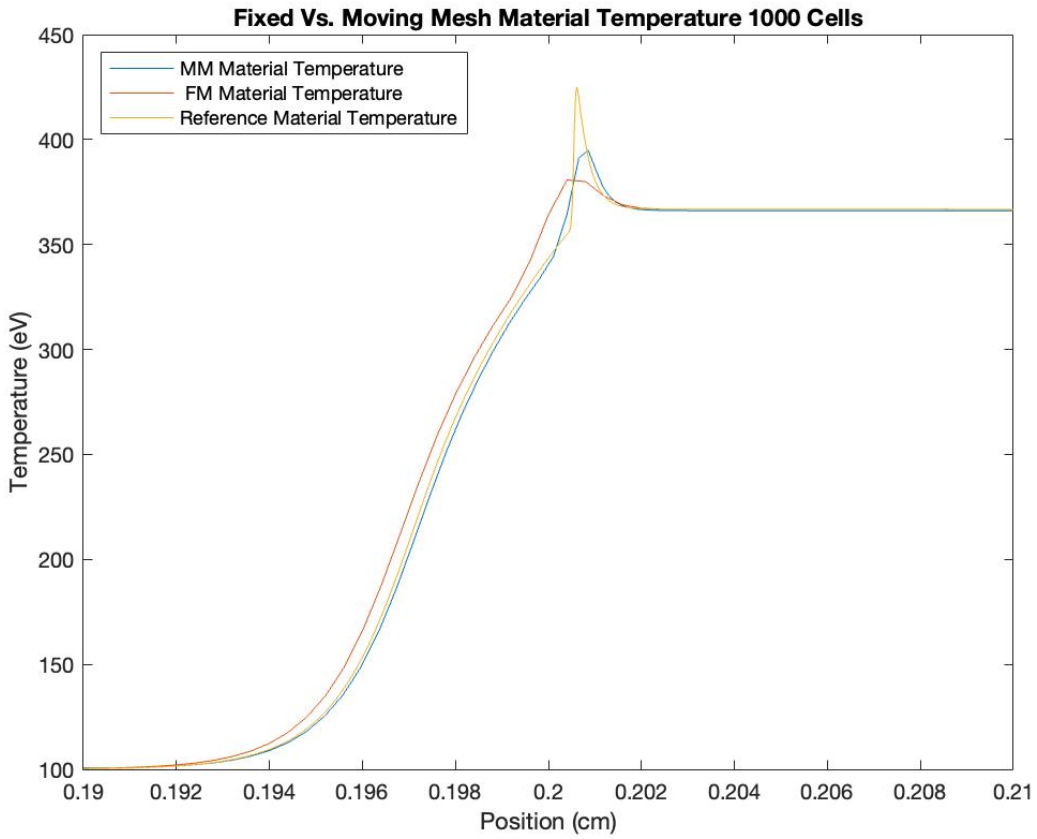


Figure 27: Material temperature for Mach 3.0 shock w/ 1000 cells.

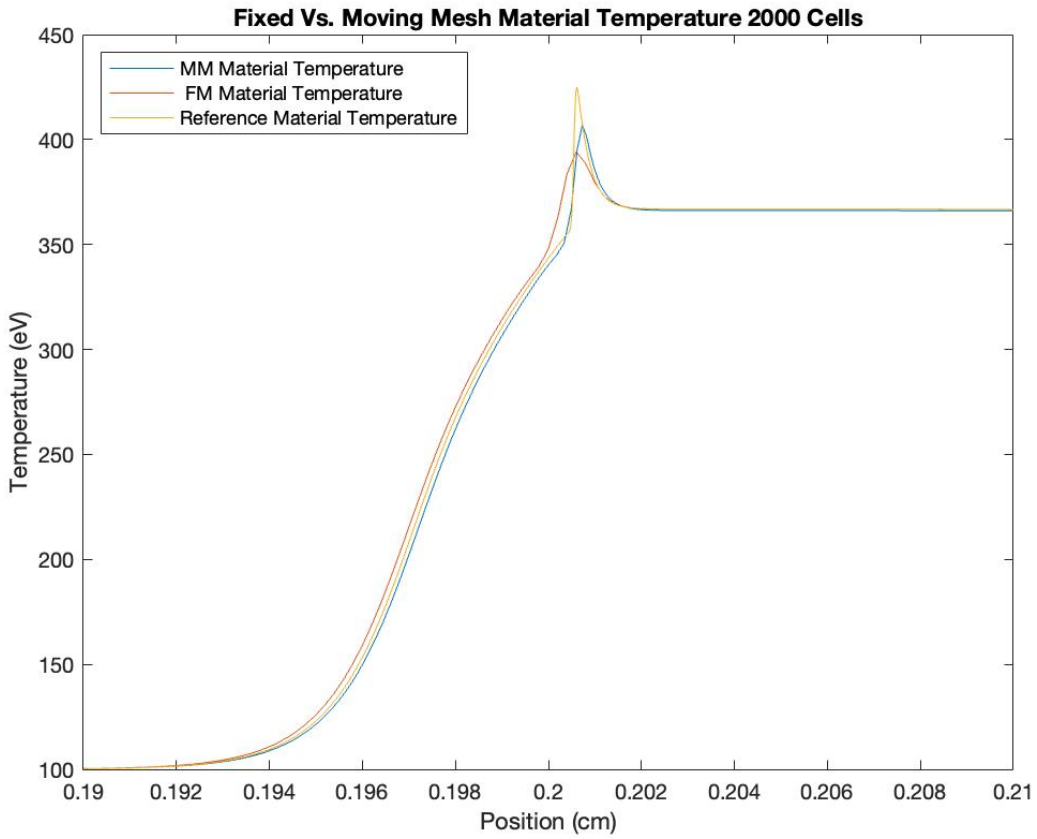


Figure 28: Material temperature for Mach 3.0 shock w/ 2000 cells.

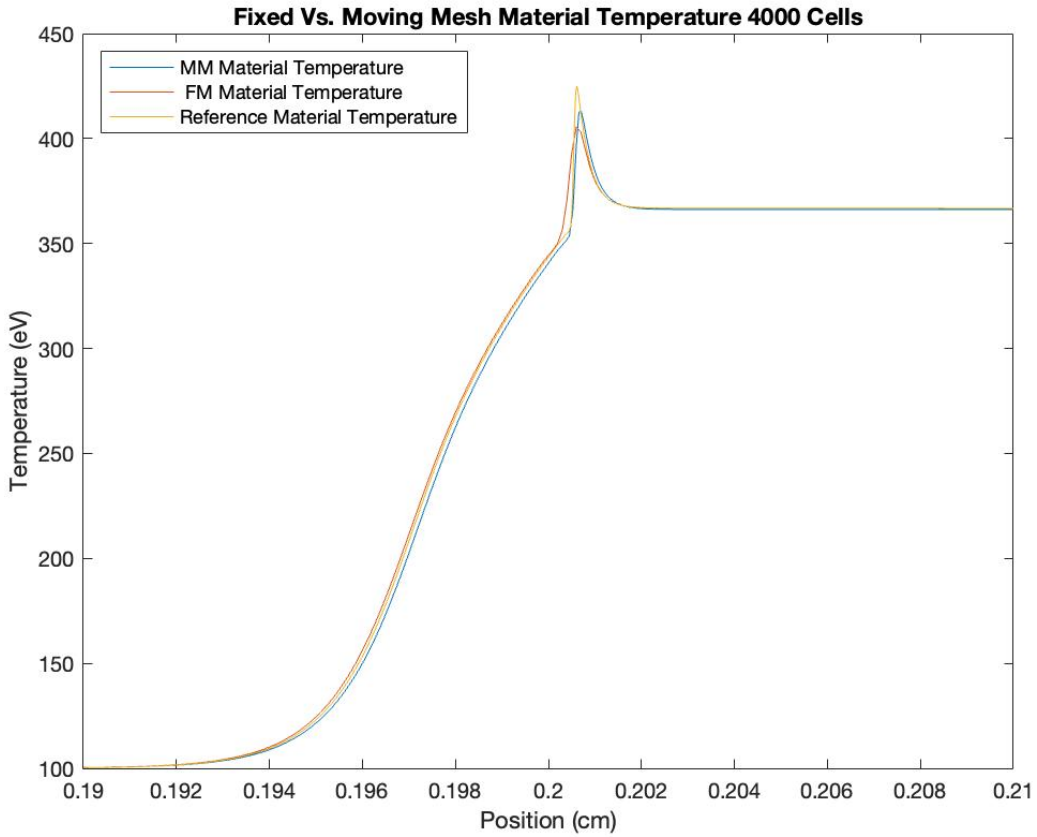


Figure 29: Material temperature for Mach 3.0 shock w/ 4000 cells.

The Material temperature for the Mach 3.0 problem demonstrates the ability of the moving mesh method to have significantly better resolution of the resolution vs. the fixed mesh method. In the coarse, 500 cell case, the moving mesh method is able to match the reference solution with much more accuracy in the precursor and shock regions. There is also some formation of a Zel'dovich spike which is not present at all in the fixed mesh solution. In fact, there is no formation of a Zel'dovich spike in the fixed mesh case until the 2000 cell case. However, with this much finer grid, the method still does not match the precursor and shock regions as well as the moving mesh case with 500 cells, and only has slightly better resolution of the Zel'dovich spike over the moving mesh with only 500 cells.

## 4.4 Moving Radiative Shocks

In the previous section the equations for the Rankine-Hugoniot jump condition for a moving shock were presented.

$$S(\rho_2 - \rho_1) = \rho_2 u_2 - \rho_1 u_1 \tag{4.4.1}$$

$$S(\rho_2 u_2 - \rho_1 u_1) = (\rho_2 u_2^2 + P_2) - (\rho_1 u_1^2 + P_1) \tag{4.4.2}$$

$$S(\rho_2 E_{h,2} - \rho_1 E_{h,1}) = (\rho_2 E_{h,2} u_2 + P_2 u_2) - (\rho_1 E_{h,1} u_1 + P_1 u_1) \tag{4.4.3}$$

$$S(\rho_2 E_{r,2} - \rho_1 E_{r,1}) = (\rho_2 E_{r,2} u_2) - (\rho_1 E_{r,1} u_1) \tag{4.4.4}$$

The shock speed to zero $S = 0$ and it was shown how to find the values in region 2 using these equations and the values in region 1. This process is the same for the moving shock; however, the shock speed can now be set to some value less than the speed of the fluid. In this report the shock speed to be set as a percentage of the fluid velocity. The jump conditions, with non-zero shock speed, can be calculated using equations 4.4.5, 4.4.6, and 4.4.7. A detailed derivation of these equations is done by Anderson in section 7.2 of *Modern Compressible Flow: With Historical Perspective* [3].

$$\frac{P_2}{P_1} = 1 + \frac{2\gamma}{\gamma + 1}\left[\left(\frac{S - u_1}{a_{s1}}\right)^2 - 1\right] \tag{4.4.5}$$

$$u_2 = u_1 + \frac{P_2 - P_1}{\rho_1 (S - u_1)} \tag{4.4.6}$$

$$\frac{\rho_2}{\rho_1} = \frac{S - u_1}{S - u_2} \tag{4.4.7}$$

The moving shock test problem will be a Mach 1.2 shock wave where the shock has a velocity of $S$. This can be set arbitrarily, but should be less than the fluid velocity of the problem. Like the stationary shock problem, $\gamma = 5/3$, $c_v = 1.4467E + 12$ erg $ev^{-1}$

$g^{-1}$, $\sigma_a = \sigma_t = 577.35\ cm^{-1}$. The density and temperature in region 1 will be $\rho_1 = 1g/cc$ and $T_1 = 100$ eV. In region 2 the temperature will be $T_2 = 120.5$ eV. The time step is $1.0E-12$ seconds and the problem runs to a final time of $1.0E-7$ seconds. The problem domain is 0.2 cm with the shock initially set at the center of the domain. A convergence study will also be performed as done with the stationary shock using 500, 1000, 2000, and 4000 cells. There is no full analytical solution to this problem, so for the convergence study the reference solution will be the fixed mesh case which was run with 15000 cells. This is a fine enough mesh for accurate results and full resolution of the shock. For the moving mesh solution, the mesh velocity will be set equal to the velocity of the shock. As discussed, this is a key advantage to the moving mesh case. Rather than having a fixed mesh or a mesh that moves with the velocity of the fluid, by setting the mesh velocity equal to that of the shock there should be an improvement in the shock resolution.

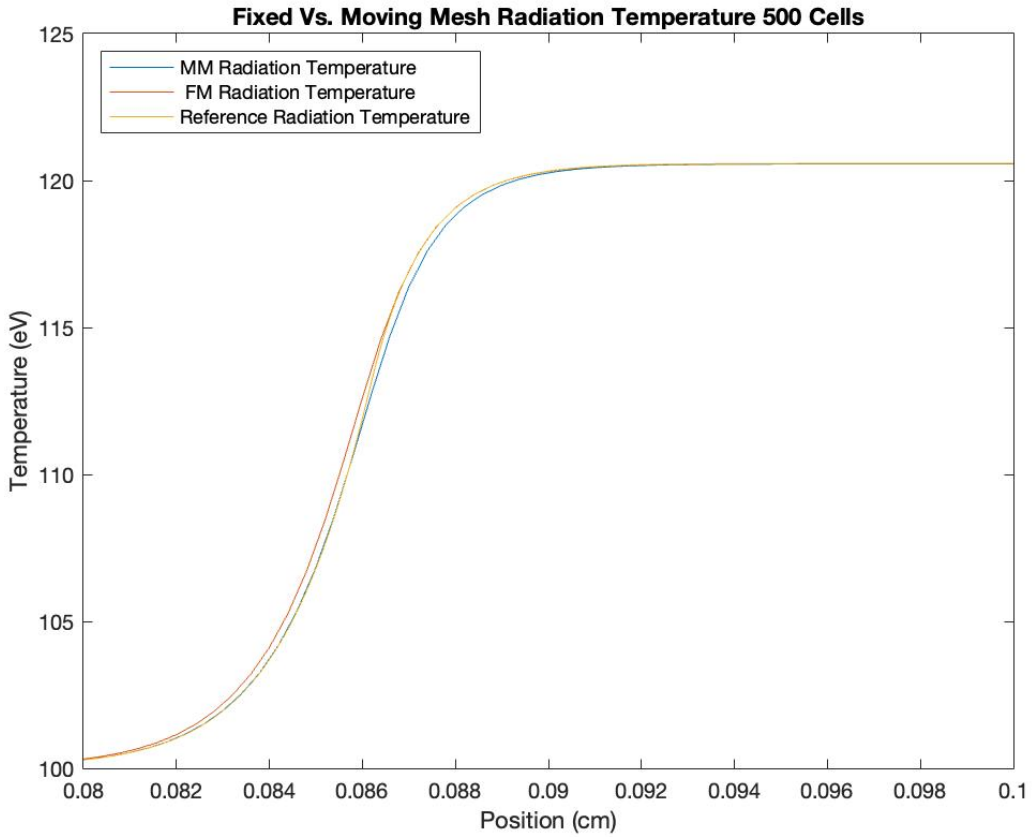


Figure 30: Radiation temperature for Moving Mach 1.2 shock w/ 500 cells.

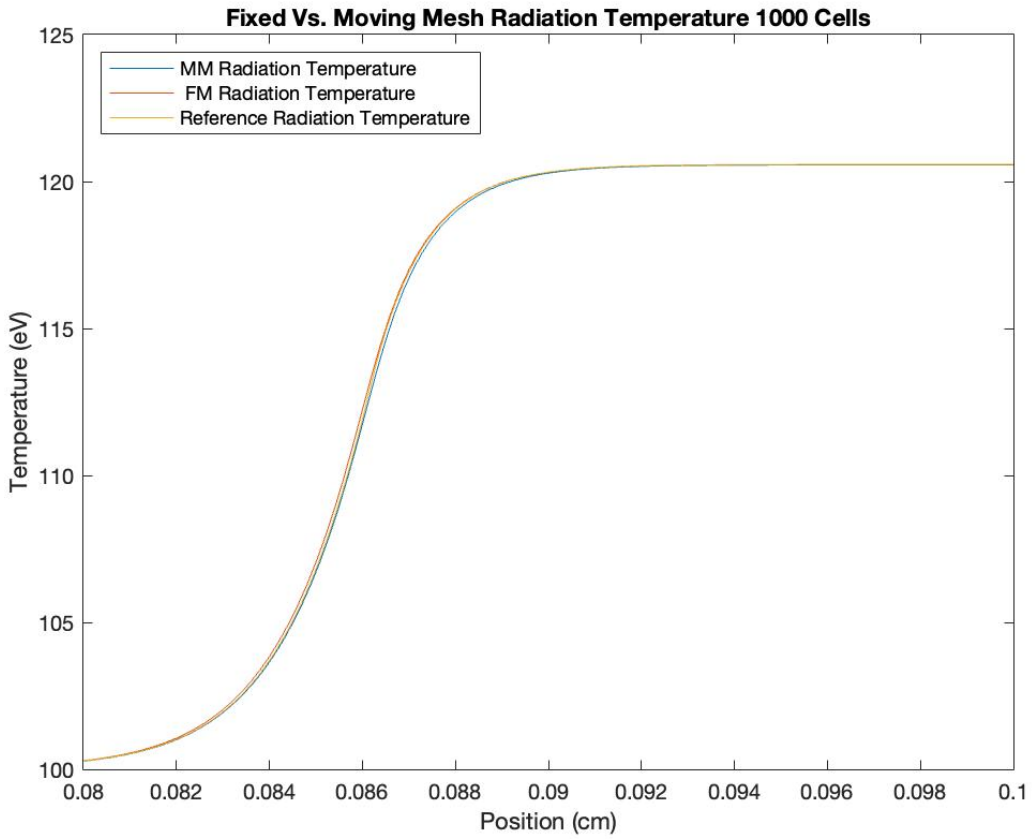


Figure 31: Radiation temperature for Moving Mach 1.2 shock w/ 1000 cells.

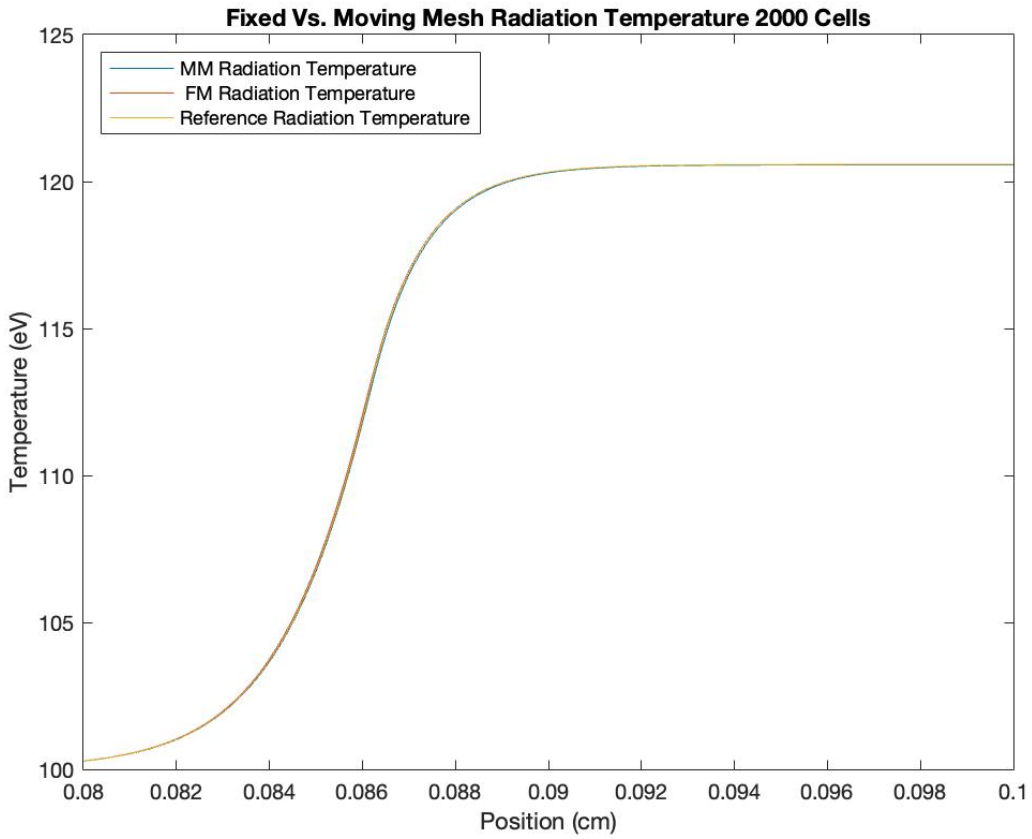


Figure 32: Radiation temperature for Moving Mach 1.2 shock w/ 2000 cells.

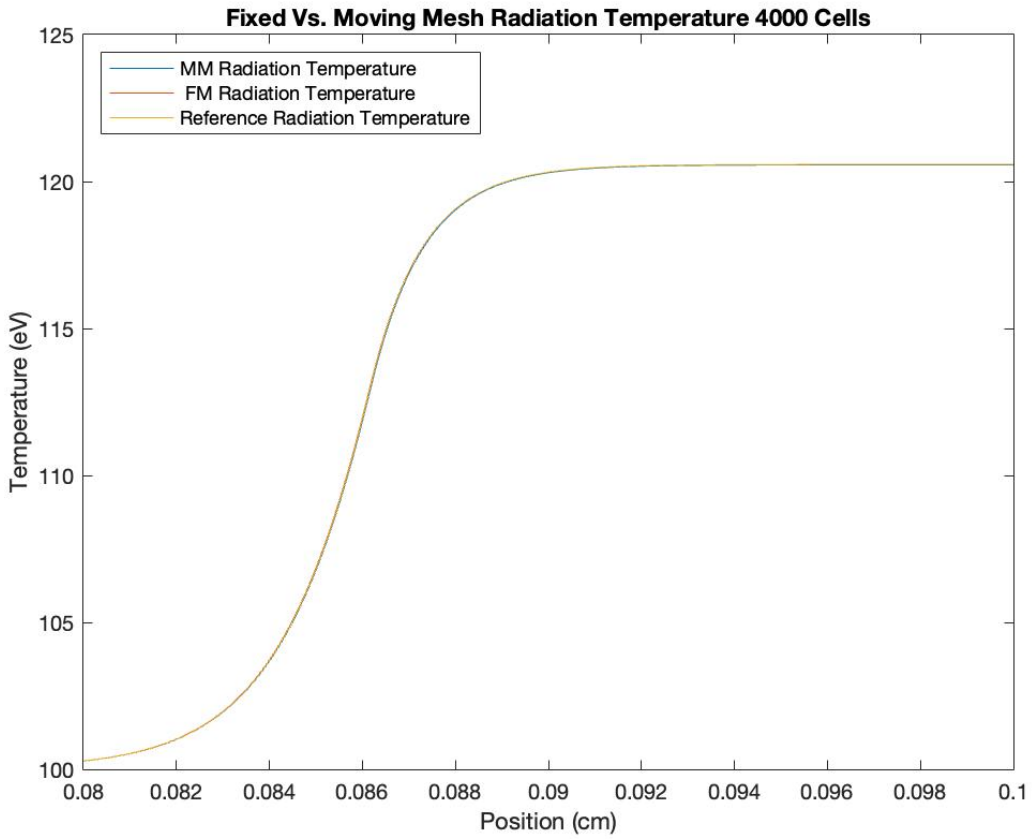


Figure 33: Radiation temperature for Moving Mach 1.2 shock w/ 4000 cells.

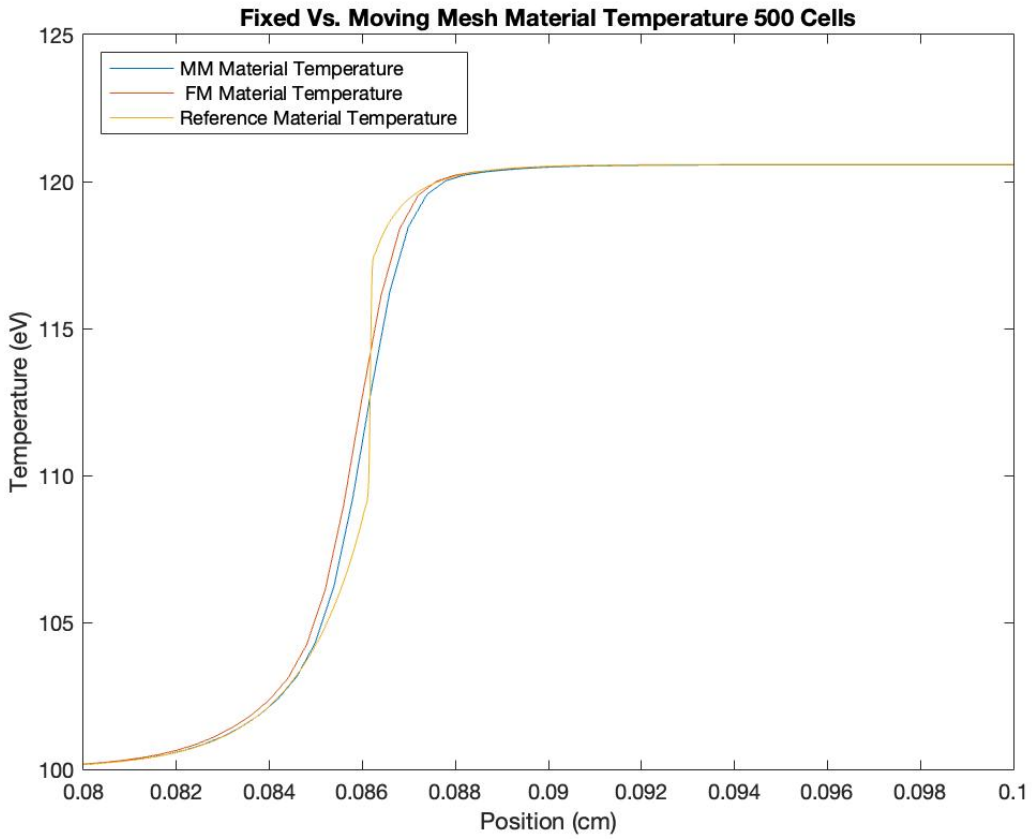


Figure 34: Material temperature for Moving Mach 1.2 shock w/ 500 cells.

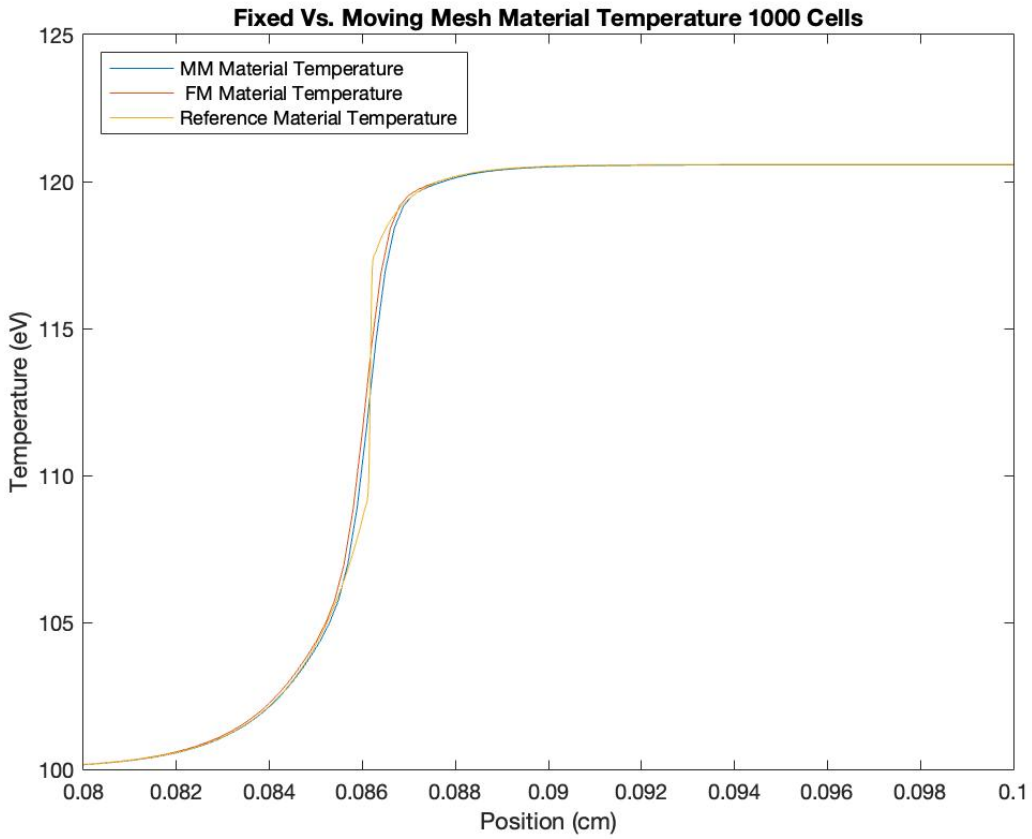


Figure 35: Material temperature for Moving Mach 1.2 shock w/ 1000 cells.

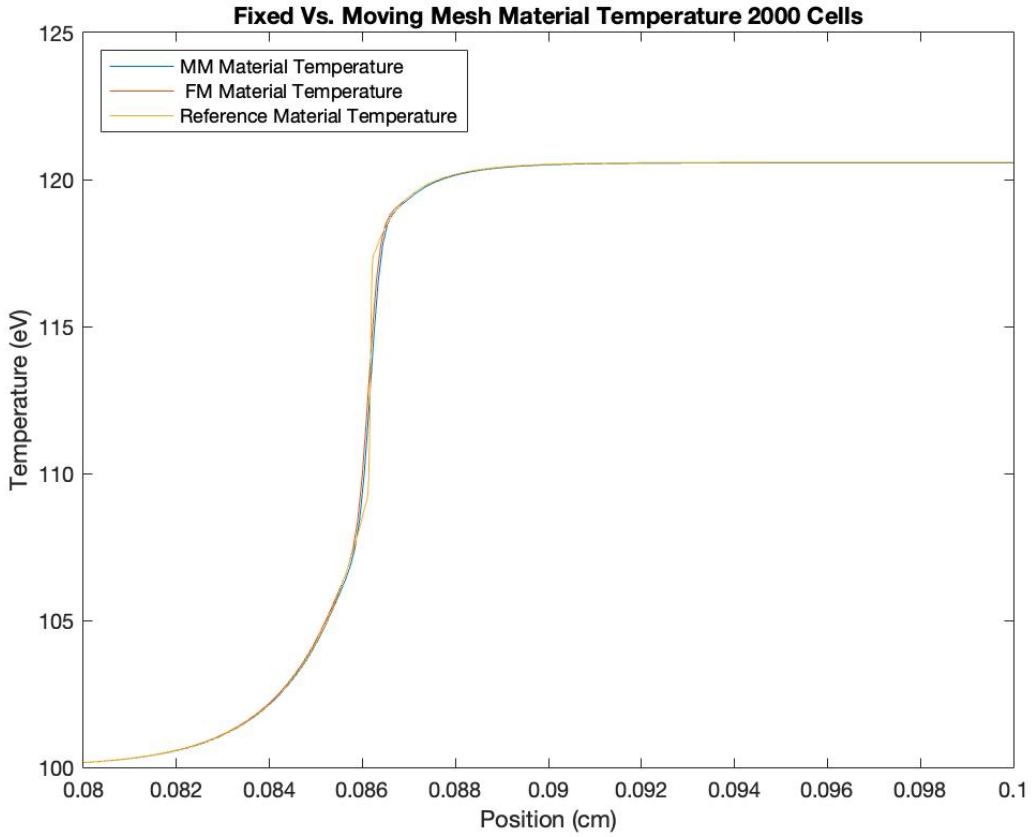


Figure 36: Material temperature for Moving Mach 1.2 shock w/ 2000 cells.

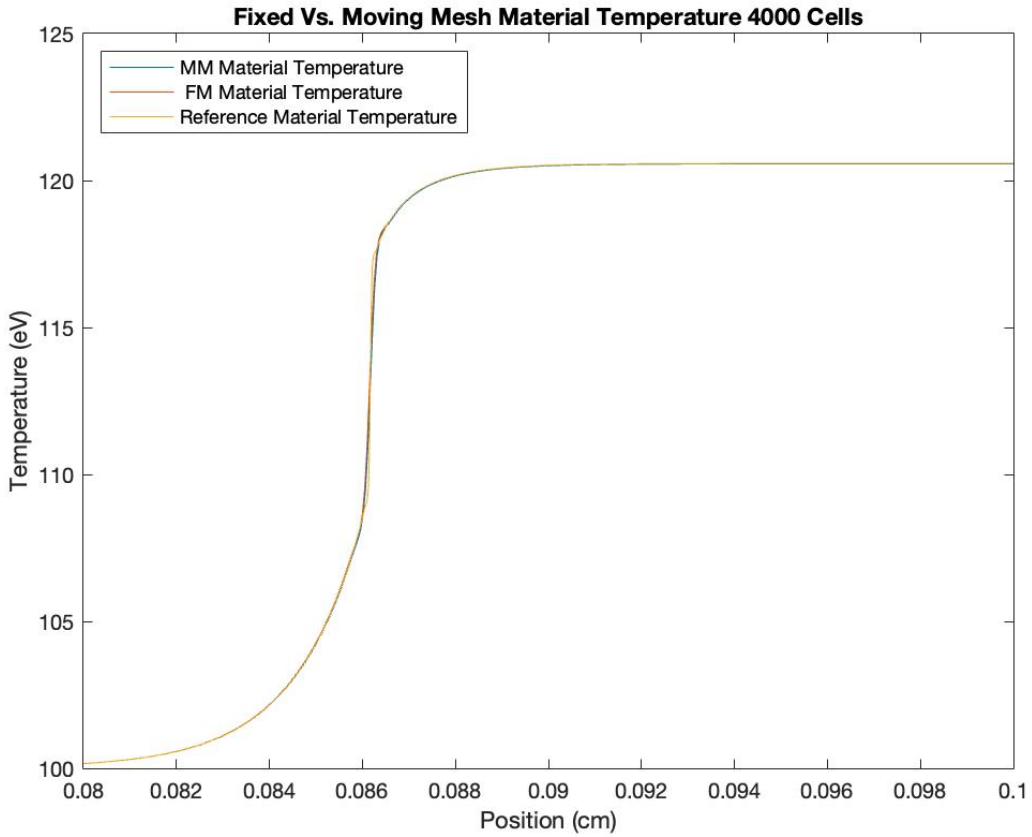


Figure 37: Material temperature for Moving Mach 1.2 shock w/ 4000 cells.

Before discussing convergence of the methods to the reference solution, the location of the shock needs to be discussed. The speed of the shock was chosen to be $S = -140109$ $cm/s$. This speed was chosen since it was slower than the speed of the fluid, but fast enough that the shock should move a significant distance by the end of the problem. The problem was ran to a final time of $1.0E-7$ seconds, and the shock was initially located at the center line of the problem which is located at 0.1 cm. From this information, it is possible to calculate that at the end the problem, which was calculated to be 0.859 cm. Looking at the plots of the material temperature, both the fixed and moving mesh methods are moving the shock to the correct location. Looking at the plots of the radiation temperature, the results are similar to that of the stationary shock Mach 1.2 problem. On the very coarse mesh containing just 500 cells, there is good resolu-

tion of the reference solution using the moving mesh method. As the mesh is further refined, both the methods are able to match the reference solution as expected. There are also similar trends in the results of the material temperature when compared to the stationary Mach 1.2 shock. On the coarse mesh solution, the moving mesh solution has better resolution in the precursor region leading up to the shock; however, both methods struggle to resolve the shock on the very coarse mesh. As the mesh is refined, both methods are able to converge to the analytical solution, with both methods producing very similar solutions with fine mesh 2000 cell and 4000 cell meshes.

# 5 Conclusions

This research aimed to develop a method that is able to more accurately model radiative shock problems than the standard fixed Eulerian mesh on coarser computational grids. The method proposed is called moving mesh Eulerian and aims to benefit from both the Eulerian and Lagrangian methods which are traditionally used. These benefits include better shock resolution, ability to handle large deformations, and the ability to handle material interfaces well. Radiative shock problems were focused on due to the presence of strong shocks in which the material is heated to a sufficiently high temperature for the radiation and kinetic energy flux to be comparable. This tests the coupling of the hydrodynamics and radiation equations, particularly the material motion correction and radiation energy deposition physics. Convergence studies were performed to see how the fixed and moving mesh methods were able to converge to a reference solution.

The initial comparison of the methods was qualitative where trends in the solutions were analyzed to see how the methods match the reference solution. From this comparison, better convergence to the reference solution was seen when using the moving mesh method over the fixed mesh method. In the slower Mach 1.2 problems, much bet-

ter convergence was achieved on the coarse grids using the moving mesh method when looking at the radiation temperatures. For the material temperature, on the coarse grid, the moving mesh method had better resolution of the precursor region, but was not able to resolve the shock. As the mesh was refined, both methods were able to converge well to the analytical solution. For the faster Mach 3.0 problem, there was a significant improvement in the solution on the coarse grid when using the moving mesh method for both the material and radiation temperature. The moving mesh solution was able to resolve the precursor, shock, and relaxation regions of the material temperature. The method also had a some resolution of the Zel'dovich spike which the fixed mesh method was unable to resolve on the coarse computational grid.

This comparison shows initially promising results for the use of the moving mesh method over the traditional fixed mesh. However, further testing should be done to determine the robustness of the method, potential time savings, and the inclusion of more complex physics within the solution of these problems. This will give more conclusive results on the abilities of the method and its potential benefits. The next section will cover this future work in detail and explain its importance to comparing the methods.

# 6 Future Work

Compared to the fixed mesh method, the moving mesh method results in better resolutions of problems containing shocks and other phenomenon that are difficult for numerical solutions to resolve. However, the current implementations of the fixed and moving mesh methods use relatively simple physics and approximations that make the problems easier to solve. To further test the benefits of accuracy and potential speed up of the moving mesh to the fixed mesh methods, the implemented physics and numerical techniques used need to be expanded. Not only will this increase the accuracy of both methods, but it will also increase the computational expense. As problems get more

computationally expensive, it will be easier to perform further studies to compare the methods.

The first step will expanding from 1-D to 2-D, and then planar to spherical geometries. The current 1-D planar geometry allowed for easier implementation and quick comparison of the methods; however, it is not physically representative of the types of problems to which these methods are applicable. By increasing to two dimensions and spherical geometry, the test problems will be physically more representative of what occurs in ICF tests. The ability to handle multiple materials problems rather than only solving single material problems will also be implemented. I also will look into second order preserving methods for the IMEX splitting of the hydrodynamics and radiative transport solutions. Lastly, I want to look into solving the full radiative transport equation rather than using diffusion theory. This will allow the use of test problems that might not be optically thick, causing the diffusion theory approximation to be inaccurate. Along with this, I will implement frequency dependence in the opacity values to account for variations in the materials optical properties over different parts of the spectrum.

Once I have expanded these methods, the process by which I compare them will be similar to the methods previously presented. I will choose a number of test problems that contain physics in which these methods should be able to accurately model. The solution gathered from the methods will then be compared to an analytical or reference solution. However, due to the additional computational complexity, I will now be able to perform speed comparisons of the methods. This will likely be done by finding some acceptable percent error to the reference or analytical solution, and then finding the number of cells that each method requires to fall within that percent error. I can then test to see potential time savings of the methods. Overall, there is still work to be done in order to further develop the moving mesh method. However, the initial results are promising.

# Appendices

## A Diffusion Approximation on Non-Uniform Grids

In section 3.4.2 the method for solving the radiation energy density on a uniform grid was presented. However, as the mesh moves, the mesh grid will deform due to differences in velocity of the fluid. The radiation solve step needs to be edited to account for these deformation in the mesh. This begins with the radiation energy density equation,

$$\frac{\partial E_r}{\partial t} = -\nabla \cdot D\nabla E_r - \sigma c E_r + \sigma a T^4 \tag{A.0.1}$$

The diffusion term is then re-written in terms of the spatial dependence $dx$.

$$\frac{\partial E_r}{\partial t} = \frac{d}{dx} - D\frac{d}{dx}E_r - \sigma c E_r + \sigma a T^4 \tag{A.0.2}$$

This equation is discretized using a backwards Euler's method taking the form shown in equation A.0.3.

$$\begin{aligned}\frac{E_{r,1}^{n+1} - E_{r,i}^{n}}{\Delta t} = \frac{1}{\Delta x_i}\left( D_{i-1/2}\left(\frac{E_i^n - E_{i-1}^n}{\Delta x_{i-1/2}}\right) - D_{i+1/2}\left(\frac{E_{i+1}^n - E_i^n}{\Delta x_{i+1/2}}\right)\right) \\ -\sigma c E_i^{n+1} + \sigma a c (T_i^4)^{n+1}\end{aligned} \tag{A.0.3}$$

where

$$\Delta x_{i-1/2} = \frac{x_i + x_{i-1}}{2} \quad \Delta x_{i+1/2} = \frac{x_{i+1} + x_i}{2} \tag{A.0.4}$$

From here is is easy to see that when the grid is uniform that $\Delta x_{i-1/2}$ and $\Delta x_{i+1/2}$ are just equal to $\Delta x_i$ which gives the $\Delta x_i^2$ term on the uniform mesh. The process of

grouping terms based on their cell index is now repeated.

$$\left(\frac{1}{\Delta t}+\frac{D_{i+1/2}}{\Delta x_i \Delta x_{i+1/2}}+\frac{D_{i-1/2}}{\Delta x_i \Delta x_{i-1/2}}\right) E_i^{n+1}-\left(\frac{D_{i+1/2}}{\Delta x_i \Delta x_{i+1/2}}\right) E_{i+1}^{n+1}- \left(\frac{D_{i-1/2}}{\Delta x_i \Delta x_{i-1/2}}\right) E_{i-1}^{n+1}=\sigma a c (T_i^4)^{n+1}+\frac{E_i^n}{\Delta t} \tag{A.0.5}$$

This gives the new equations for the diagonals of the tri-diagonal matrix $a$, $b$, $c$, and $d$. The radiation energy density can now be solved for using the Thomas Algorithm presented earlier.

$$a_i=-\frac{D_{i-1/2}}{\Delta x \Delta x_{i-1/2}} \tag{A.0.6}$$

$$b_i=\frac{1}{\Delta t}+\frac{D_{i+1/2}}{\Delta x_i \Delta x_{i+1/2}}+\frac{D_{i-1/2}}{\Delta x_i \Delta x_{i-1/2}} \tag{A.0.7}$$

$$c_i=-\frac{D_{i-1/2}}{\Delta x_i \Delta x_{i-1/2}} \tag{A.0.8}$$

$$d_i=\sigma a c (T_i^k)^4+\frac{E_i^n}{\Delta t} \tag{A.0.9}$$

# B Fixed Mesh Eulerian Code

The code for the fixed mesh Eulerian method can be found at https://github.com/dweatherred/Rad-Hydro. Please reach out with any question or concerns regarding running the code.

# C Moving Mesh Eulerian Code

The code for the moving mesh Eulerian method can be found at https://github.com/dweatherred/MM_Rad_Hydro. Please reach out with any question or concerns regarding running the code.

# References


[1] *An Assessment of the Prospects for Inertial Fusion Energy.* The National Academies Press, Washington, DC, 2013.

[2] Basic Fusion Physics. *International Atomic Energy Agency*, October 2016.

[3] J.D. Anderson. *Modern Compressible Flow: With Historical Perspective.* Aeronautical and Aerospace Engineering Series. McGraw-Hill Education, 2003.

[4] U. M Ascher, S. J. Ruuth, and R. J. Spiteri. Implicit-Explicit Runge-Kutta Methods for Time-Dependent Partial Differential Equations. *Applied Numerical Mathematics*, 1999.

[5] B. Bishop. National Ignition Facility Achieves Fusion Ignition. LLNL Report, Lawrence Livermore National Laboratory, 2022.

[6] John Castor. *Radiation Hydrodynamics.* Cambridge University Press, 2004.

[7] Philip Chang, Shane W Davis, and Yan-Fei Jiang. Time-Dependent Radiation Hydrodynamics on a Moving Mesh. *Monthly Notices of the Royal Astronomical Society*, 493(4):5397–5407, 02 2020.

[8] Avner P. Cohen and Shay I. Heizler. Modeling of Supersonic Radiative Marshak Waves Using Simple Models and Advanced Simulations. *Journal of Computational and Theoretical Transport*, 47(4-6):378–399, sep 2018.

[9] J. A. Glaze. Shiva: A 30 Terawatt Glass Laser for Fusion Research. Presented at ANS Ann. Meeting, San Diego, Calif., 18-23 Jun. 1978, feb 1978.

[10] A. C. Hayes, G. Jungman, J. C. Solem, P. A. Bradley, and R. S. Rundberg. Prompt Beta Spectroscopy as a Diagnostic for Mix in Ignited NIF Capsules. *Modern Physics Letters A*, 21(13):1029–1040, apr 2006.

[11] S. Y. Kadioglu, D. A. Knoll, R. B. Lowrie, and R. M. Rauenzahn. A Second Order Self-Consistent IMEX Method for Radiation Hydrodynamics. *Journal of Computational Physics*, 2010.

[12] Rahul Kannan, Mark Vogelsberger, Federico Marinacci, Ryan McKinnon, Rüdiger Pakmor, and Volker Springel. arepo-rt: Radiation Hydrodynamics on a Moving Mesh. *Monthly Notices of the Royal Astronomical Society*, 485(1):117–149, 2019.

[13] Randall J. LeVeque. *Finite Volume Methods for Hyperbolic Problems*. Cambridge Texts in Applied Mathematics. Cambridge University Press, 2002.

[14] R. E. Marshak. Effect of radiation on Shock Wave Behavior. *Physics of Fluids*, 1, January 1958.

[15] Mihalas B. W. Mihalas, D. *Foundations of Radiation Hydrodynamics*. Oxford University Press, 1984.

[16] John H. Nuckolls. Early Steps Towards Inertial Fusion Energy (IFE) (1952 to 1962). LLNL Report UCRL-ID-131075, Lawrence Livermore National Laboratory, 1999.

[17] Gerald Pomraning. *The Equations of Radiation Hydrodynamics*. Pergamon, Headington Hill Hall, Oxford, 1973.

[18] W. H. Press, S. A. Teukolsky, W. T. Vetterling, and B. P. Flannery. *Numerical Recipes in C++ (Vol. 2)*. Cambridge Univ. Press, 2002.

[19] Gary A Sod. A Survey of Several Finite Difference Methods for Systems of Nonlinear Hyperbolic Conservation Laws. *Journal of Computational Physics*, 1978.

[20] Volker Springel. E pur si muove: Galilean-Invariant Cosmological Hydrodynamical Simulations on a Moving Mesh. *Monthly Notices of the Royal Astronomical Society*, 401(2):791–851, 01 2010.

[21] Bram van Leer. Towards the Ultimate Conservative Difference Scheme. V. A Second-Order Sequel to Godunov's Method. *Journal of Computational Physics*, 32(1):101–136, 1979.

[22] H. K. Versteeg and W. Malalasekera. *An Introduction to Computational Fluid Dynamics*. Pearson Education Limited, 1995.

[23] Eric W. Weisstein. *Predictor-Corrector Methods*. MathWorld, 2011.